

Seismically induced rockfall hazard from a physically based model and ground motion scenarios in Italy

Massimiliano Alvioli^{*1}, Gaetano Falcone^{2,3}, Amerigo Mendicelli², Federico Mori², Federica Fiorucci¹, Francesca Ardizzone¹, and Massimiliano Moscatelli²

¹Consiglio Nazionale delle Ricerche, Istituto di Ricerca per la Protezione Idrogeologica, via Madonna Alta 126, I-06128, Perugia, Italy

²Consiglio Nazionale delle Ricerche, Istituto di Geologia Ambientale e Geoingegneria, Area della Ricerca di Roma 1, Via Salaria km 29.300, 00015 Monterotondo (Roma), Italy

³DICATECh—Dipartimento di Ingegneria Civile, Ambientale, del Territorio, Edile e di Chimica, Politecnico di Bari, via Orabona 4, Bari, 70125, Italy

Abstract

The majority of landslide susceptibility and hazard zonation are implemented with statistical methods, especially on large scales: mostly because the data needed for physical simulations are only available in small areas. Physically-based simulations for slope stability are conceptually different from widely used statistical approaches. Both methods have specific advantages, depending on available data, their type and resolution, and the aim of the study. Here, we perform a hazard zonation based on the physical model STONE for the simulation of rockfalls, at 10 m resolution consistently all over Italy, and aggregating results at the slope unit level. The novelties, here, are: (i) the introduction of a seismic trigger for rockfalls, which adds a temporal component to an intrinsically static model and allows to obtain an estimate of seismically induced rockfall hazard, (ii) high-resolution application of the model at national scale, and (iii) implementation of the results in a WebGIS. Peak ground acceleration maps with different return times including seismic amplification represent the earthquake trigger. A data-driven map of possible rockfall sources all over Italy, mapped by experts in sample representative locations, allowed statistical generalization to unsurveyed areas, at national scale. Eventually, application of a simple linear transformation, to map values of peak ground acceleration into activation probability of sources, links “static” rockfall simulations with “dynamic”, time-dependent triggering. Results are maps of rockfall susceptibility with different return times, *i.e.*, a step forward to the full assessment of rockfall hazard. Maps of hazard values and corresponding uncertainties, aggregated at slope unit level and categorized, are readily available for download, and for visualization in the new WebGIS. The new model for seismic triggering of rockfalls can be applied at the local and regional scale, calibrated with specific earthquake events instead of the return time scenarios considered here. On the temporal scale, this approach is suited for application in near-real time.

Keywords: Rockfalls, Seismically induced landslides, Ground motion, Shake maps, Slope Units

Highlights

- We perform physical rockfall simulations at 10 m resolution all over Italy
- A novel seismic trigger mechanism adds a dynamic component to the static model
- Seismic shake maps for different return times help calibrating a dynamic trigger
- Susceptibility maps for different return times are a new step towards rockfall hazard

Contents

1	Introduction	2
2	Background	2
3	Materials	3
3.1	Data	3
3.2	Software	4
3.3	Study area	5
4	Methods	7
4.1	Optimized slope unit delineation	7
4.2	Simulation of rockfall trajectories with STONE	7
4.3	Scenarios for peak ground acceleration	9
4.4	Seismic triggering of rockfall sources	10
5	Results	11
6	Discussion	15
7	Conclusions	18
8	Data availability	21
9	Acknowledgments	21

*Correspondence: massimiliano.alvioli@irpi.cnr.it

1 Introduction

Co-seismic landslides are long recognized as one of the most prominent ground effects of earthquakes, besides deformations, liquefaction, and surface faulting, resulting from ground shaking due to the propagation of seismic waves (Keefer, 2002). Waves propagate in all directions from the epicenter of the earthquake and ground effects can occur at considerable distance from the initial surface rupture (Dai et al., 2011; Pokharel et al., 2021). Assessment of the distribution of landslides caused by a specific earthquake, their number, size and runout distance is key to infer the secondary hazard posed by landslides triggered by an earthquake (Harp et al., 2011; Fan et al., 2019).

As most earthquake-induced landslides in Italy are rockfalls (Martino et al., 2014; Caprari et al., 2018; Romeo et al., 2017), in this work we adopted a specific physically based model to describe this kind of landslides. A rockfall is a rock block detached from a cliff by sliding, toppling or falling, and subsequently falling independently. It falls along a vertical or sub-vertical slope by bouncing and flying along ballistic trajectories, or by rolling on talus. The block motion comes to an end when it has lost all of its energy during impacts or by friction. Here, we describe rockfall trajectories using a simple three-dimensional program called STONE, developed two decades ago by Guzzetti et al. (2002). The model is typically used for rockfall susceptibility or risk assessment on specific sites/infrastructure (Guzzetti et al., 2003, 2004; Santangelo et al., 2019; Alvioli et al., 2021).

The main novelty introduced in this work is a mechanism to combine information from static, time— and trigger-independent potential rockfall sources, with scenarios for peak ground acceleration (PGA) due to seismic shaking including ground motion modifications induced by sub-soil site condition. This allows obtaining probabilistic maps of seismically-induced rockfall sources, linked to a given return time, corresponding to the return time associated with the selected PGA scenarios. Thus, the link between a seismic trigger with given return time effectively adds a temporal component to the static model.

The method, in turn, assumes knowledge of pre-existing conditions for the possible detachment of a block, which we establish in a probabilistic way based on sole morphometric considerations (Alvioli et al., 2021). The process of detachment of blocks due to ground shaking is a complex one (Huang et al., 2011), and the method presented here is the simplest yet effective way we could devise to link ground shaking and rockfall triggering. Simulations of rockfall trajectories initiated from the triggering locations result in maps representing the spatial likelihood of rockfall occurrence.

On the other hand, the model does not explicitly provide a quantitative measure of the magnitude of expected events;

each simulated trajectory does not embed information on the size, or destructive power, of the falling block. Thus, considering spatial distribution of PGA values corresponding to earthquake events with given return times, we eventually obtain an overall assessment for seismically-induced landslide hazard at national scale, in Italy, excluding the magnitude of such events.

Results of this work are aggregated at slope unit level. Examples of landslide studies based on the same national slope unit map exist in the literature. They discussed a conceptual debris flow model (Marchesini et al., 2020), rockfall susceptibility using STONE but no specific trigger (Alvioli et al., 2021), artificial neural networks (Amato et al., 2021) and a statistical model for landslide susceptibility for different landslide types in Italy (Loche et al., 2022a).

This work is organized as follows. **Section 2** provide motivations and a brief review of literature relevant to co-seismic landslide hazard, and rockfall hazard. **Section 3** lists and briefly describes the data used here, in **Section 3.1**, the software used for the completion of this work, in **Section 3.2**, and the details of the study area, in **Section 3.3**. **Section 4** describes the basics of the approach adopted here, and it is organized in subsections corresponding to the different steps of our approach. **Section 5** illustrates the results obtained for earthquake-induced rockfall hazard, while **Section 6** contains a critical discussion of the results and **Section 7** lists the conclusions that can be drawn. The maps obtained in this work are available for download and visualization in a WebGIS, as described in **Section 8**.

2 Background

Post-seismic landslides may occur well after the event and considerable effort has been devoted to the study of their residual hazard (Yamaguchi and Kasai, 2022; Loche et al., 2022b). Landsliding frequency increases after a large earthquake, and the effect may persist for years, or decades (Marc et al., 2015; Massey et al., 2022). Complete landslide hazard assessment requires the joint knowledge of the spatial likelihood of occurrence (susceptibility), of its magnitude, and of its temporal dependence (Nadim, 2013; Alvioli et al., 2018). Specifically, rockfalls are among the most prominent types of landslides caused by earthquakes, with examples in many earthquake- and rockfall-prone areas of the world (Wick et al., 2010; Massey et al., 2014), also from events in the past (Owen et al., 2008; Fernández et al., 2021). One limitation in explicitly dealing with rockfalls is that landslide inventories often do not distinguish the different types of landslides.

The literature contains a vast body of work about earthquake-induced landslide susceptibility. Recent studies feature statistical methods with a variable selection

of spatial predictors, and a few predictors associated to specific earthquake events. The latter may be intended as dynamic predictors, to mimic temporal dependence of the action of seismic shaking on pre-existing, static terrain conditions (Nowicki Jessee et al., 2018; Tanyaş et al., 2019a; Valagussa et al., 2019). Dynamic predictors represent quantitative measures of earthquake intensity; examples are peak ground acceleration, peak ground velocity, or modified Mercalli intensity. Variations of such methods were devised to incorporate the magnitude of landslide distribution (Tanyaş et al., 2019b).

Nevertheless, a truly time-dependent approach requires considerable additional information, to account for different possible events with different characteristics of ground shaking scenarios. This can be accomplished by stochastic simulations based on sophisticated statistical analysis (Lombardo and Tanyaş, 2021). A totally different approach – adopted in this work – stems from the use of physically based models for the description of landslide occurrence. Most physically based models embed both spatial and time dependence and, in principle, they may be a good fit for the assessment of landslide hazard, provided a sound mechanism to link seismic shaking and landslide triggering can be devised.

One existing method to describe co-seismic slope behavior is the rigid-block method of Newmark (see Wang et al. (2016) for the case of the Wenchuan earthquake, and references therein), which considers the friction of blocks sliding on an inclined plane when subject to accelerations due to ground shaking. The method is typically used to estimate displacements of different locations hit by earthquakes, and displacements rates may be related to the rate of occurrence of landslides/rockfalls, provided sufficient data is available for calibration. We did not consider this approach, here.

The model STONE, adopted here to describe rockfalls trajectories, does not contain a temporal component, nor does it implement seismic shaking as an input for the initiation of rockfalls. It just calculates geometric trajectories for given starting points, or sources. Thus, to use the model in combination with ground motion scenarios, one solution is to prepare different input source maps for different earthquake scenarios. This also allows including the effect of stratigraphic amplification (Assimaki et al., 2005); we did not include topographic amplification, instead (Pignatola et al., 2022). Examples exist of accurate analysis of predisposing factors to investigate the likelihood of rock faces to be destabilized by ground shaking (Huang et al., 2011; Mavrouli et al., 2009).

To the best of our knowledge, all of the existing models comparable with STONE (RockGIS, (Matas et al., 2017); Rockyfor3D, (Dorren et al., 2022) and references therein; 2D CRSP, (Jones et al., 2000) require very similar input, and embed no triggering mechanism. In the case of CRSP, recently Kanari et al. (2019) inves-

tigated the relationship between the blocks’ initial velocity and PGA values, and concluded that the initial velocities are almost irrelevant, as far as the blocks’ travel distance is concerned. The same holds true for STONE (which we checked), in which initial velocity can be configured; this is the main reason why we devised a different way to relate PGA and triggering probability.

An example of rockfall hazard calculated using a three-dimensional model, branched from STONE and called Hy-STONE (Agliardi and Crosta, 2003), was applied in Italy for the Friuli Earthquake of 1976 (Valagussa et al., 2014). In that case, the authors included magnitude estimated from frequency–size relationship of rockfalls in the study area, and used seismic-hazard scenarios with different annual frequencies of occurrence. The probability of rockfall triggering was obtained with a discriminant function analysis using slope and PGA as input variables. The model applied here is simpler than the referenced one – but it has the advantage of using amplified PGA *i.e.*, PGA at flat outcropping intact rock modified by the local site conditions), and of being applicable to an area as large as the whole of Italy, with the potential of being further developed in a near-real time approach.

3 Materials

Here we describe materials used to generate PGA maps, to perform simulations of rockfall trajectories, and to aggregate and visualize results – separately for data and software.

3.1 Data

The PGA maps used in this work, developed by Falcone et al. (2021) and Mendicelli et al. (2022), exploited a large database of seismic microzonation data published by the Italian Civil Protection Department (Benigni et al., 2018) and from the Italian Institute of Geophysics and Volcanology (INGV). The data included:

- A set of about 40,000 continuous boreholes, useful to define lithological successions existing in Italy.
- About 1,200 down-hole seismic tests and 3,000 multichannel analysis of surface waves, which were associated with soil covers (*i.e.*, clay, sand, and gravel) and geological bedrock recognized from about 4,200 borehole logs. The data allowed extraction of profiles for the shear wave velocity, V_S , and the average shear wave velocity of the upper 30 m, V_{S30} , for each lithotype of interest (Mori et al., 2020). For the same purpose, additional data were retrieved from literature, such as the decay of secant shear modulus according to the shear strain increase (see Falcone et al. (2021), and references therein).
- Acceleration response spectra in Italy, obtained from the reference seismic hazard corresponding to 475 y

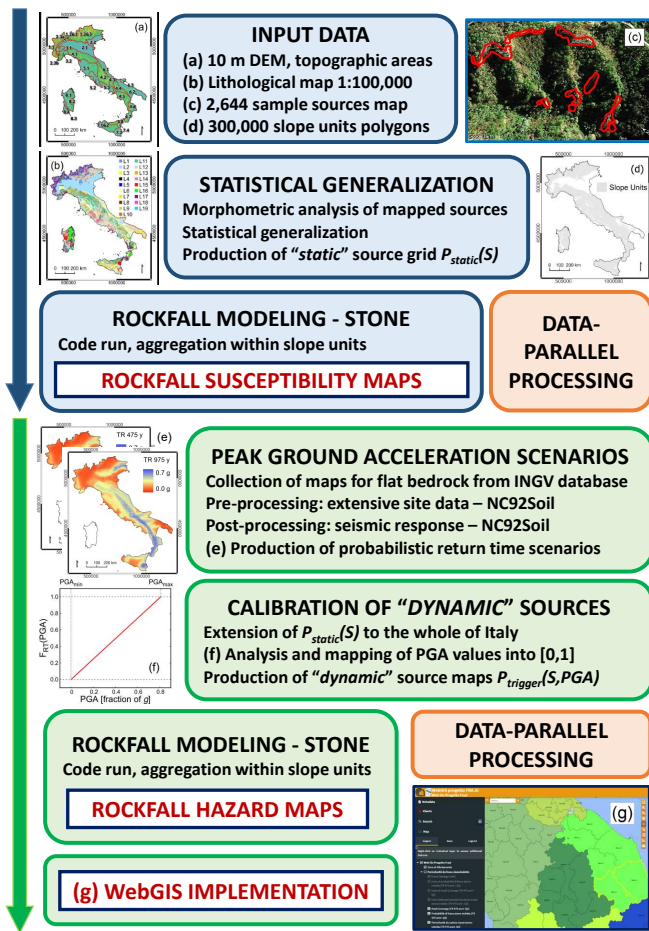


Figure 1: A diagram representing the overall framework for the production of rockfall hazard maps. The upper part of the diagram (maps and boxes in blueish colors) describes the ingredients needed to perform this study, obtained from previously published work; the lower part (maps and greenish colors) shows the activities specifically developed and implemented for this work, as far as rockfall modeling is concerned. See Fig. 2 for a larger version of the thumbnails in (a) and (b).

and 975 y return periods (Meletti and Montaldo, 2007; Montaldo and Meletti, 2007). These are two of the nine return times available from the INGV website.

Section 4 describes how the data above were useful to obtain PGA maps for the two return periods, 475 y and 975 y, considered in this work.

Data used to perform rockfall simulations with STONE are as follows. Inputs of the code are a digital elevation model (DEM), a map of rockfall sources at the same resolution of the DEM, and maps containing numerical values of parameters used in the code. The method presented in this paper builds on the application described by Alvioli et al. (2021). In the cited work, the model STONE was still applied at national level, but limited to a buffer

around the railway network (about 24,000 km²), and regardless of any particular trigger.

Here, we applied the same code for rockfall trajectory simulation on all of Italy, instead (about 240,000 km²); we also extended the same method for the probabilistic localization of potential rockfall sources, subject to the further constraint of selective activation on the basis of different PGA values. Thus, in addition to the PGA maps corresponding to different return time scenarios, we used the same input data as in Alvioli et al. (2021), namely:

- A DEM with national coverage, with 10 m grid size, named TINITALY (Tarquini et al., 2007) (shown in Fig. 1(a) and Fig. 2(a), along with a map of subdivision in physiographic units of Italy (Guzzetti and Reichenbach, 1994));
- A lithological map of Italy, scale 1:100,000, containing 19 lithological classes and developed specifically for the purpose of aiding physically-based slope stability assessment (Fongo, 2018; Bucci et al., 2022). Each lithological unit in the map was associated to specific range of input parameters of the code STONE, namely friction (dynamic parameter, relevant to the rolling state of masses, in STONE) and normal and tangential restitution (relevant for the bouncing impacts on the ground). Numerical values are listed in Table 1; a map is in Fig. 1(b) and Fig. 2(b).
- A map of sample potential source area for rockfalls in Italy, from expert interpretation of Google Earth™ images. A detailed description of the mapping criteria and of the relevance of such map for building a probabilistic model of rockfall sources, of course, is in Alvioli et al. (2021) and will be briefly summarized in Section 4.4; a sample Google™ image with a small sample of expert-mapped polygons is in Fig. 1(c).
- A national slope unit map (Alvioli et al., 2020), containing more than 300,000 slope unit polygons, of variable shape and size, generated with the software r.slopeunits (Alvioli et al., 2016). Slope units exclude plains and cover 224,000 km², out of the the total area of Italy, about 300,000 km²; a thumbnail image showing overall coverage of slope units is in Fig. 1(d).
- An inventory of seismically-induced landslides, collected by the *Centro di Ricerca per i Rischi Geologici* (CERI), and called *Catalogo degli Effetti Deformativi al suolo Indotti da forti Terremoti in Italia* (CEDIT), consisting of 2,058 landslide points and used for partial validation in this work.

3.2 Software

Most of the GIS analyses described in this work were performed in GRASS GIS running in a Linux OS, with ex-

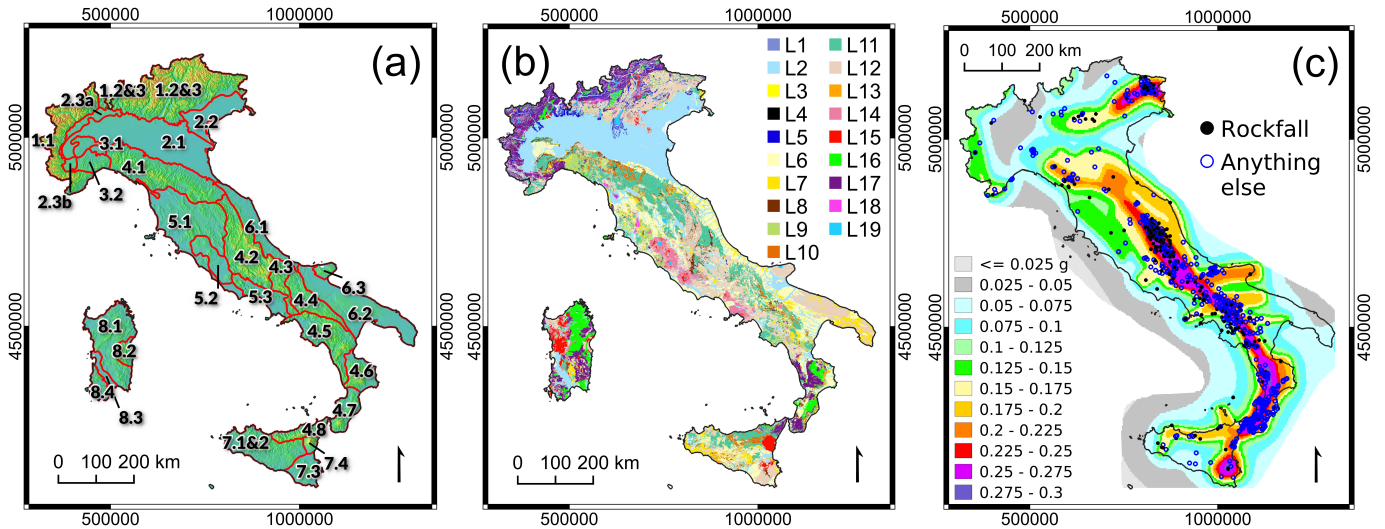


Figure 2: The physiographical, topographical, lithological settings of Italy and relationships with seismic hazard and seismic ground effects. (a) Subdivision in physiographic areas (originally defined by **Guzzetti and Reichenbach (1994)** and further modified by **Alvioli et al. (2021)**), consisting of eight main provinces and further split in a total of 29 sections (*cf.* **Table 2**); the underlying topography elevation is also shown. (b) Lithological map recently obtained by **Bucci et al. (2022)**, at the scale 1:100,000, containing 19 classes (*cf.* **Table 1**). (c) Seismic hazard levels in Italy, represented by maximum ground acceleration with exceeding probability of 10% in 50 years (**Stucchi et al., 2004**); full black dots are seismic-induced rockfalls (1100), while blue circles are any other type of landslides (1606, of which 475 of unknown type; from CEDIT database (**Martino et al., 2014; Caprari et al., 2018**)).

tensive use of bash scripting and parallel computing. The national slope unit map was obtained previously using the `r.slopeunits` module, by **Alvioli et al. (2016)**; the optimization procedure and scripts were updated as in **Alvioli et al. (2020); Pokharel et al. (2021)**. The maps of expected peak ground acceleration were obtained using the `NC92Soil` software (**Falcone et al., 2021**). Simulations of rockfall trajectories were obtained using the software `STONE` (**Guzzetti et al., 2002**), parallelized in a data-distributed framework using scripts originally developed by **Alvioli et al. (2021)**. Visualization in a WebGIS required the software `G3W-SUITE`, a modular client-server application based on `QGIS-Server` for the publication of interactive cartographic projects, compatible with `QGIS 3.16 LTR`.

3.3 Study area

The area studied in this work is the boot-shaped Italian peninsula, consisting of about 300,000 km², located in southern Europe. Italy has two main mountain ranges; the Apennines, crossing the peninsula roughly from North to south, and the Alps, of which Italy contains the southern parts. The largest plain is the Po Valley and the two major island are Sicily and Sardinia. The physiographic setting of Italy was nicely summarized by the classification of **Guzzetti and Reichenbach (1994)**, who distinguished eight main physiographic provinces (*cf.* **Fig. 2**), namely: 1., Alpine Mountain System; 2., North Italian Plain; 3., Alpine-Apennines Transition Zone; 4., Apennine Mountain System; 5., Tyrrhenian Borderland; 6., Adri-

atic Borderland; 7., Sicily; 8., Sardinia. They are further split in a total of 29 (originally 30) sub-units (sections), describing the general topographic and geomorphological diversity of Italy. The boundaries between provinces are easily traced and correspond to major morphological, geological and coastline features, while the borders of sections are distinct and generally more open to interpretation (**Guzzetti and Reichenbach, 1994**). More recently, the physiographic sections were considered for further classifying Italy into topographic-morphologic clusters using hydrological basins as the basic classification unit; the interested reader is referred to **Alvioli et al. (2020)** for further details and results. **Figure 2(a)** shows a full-size version of the thumbnail of physiographic zones in **Fig. 1(a)**, overlaid to a shaded relief map. The physiographic zones correspond with the ones listed in **Table 1**.

Italy contains a large variety of geological features, approximately corresponding with the physiographic classification given above. The country is in active geodynamic evolution, resulting in volcanoes, earthquakes, and widespread land and coasts instability. Geology in the area is controlled by the progressive approaching of two megaplates, Eurasia to the north and Africa to the south. The geology of Italy is remarkably varied and contains rock series from all eras and periods (**Bosellini, 2017**). The Alps chain are a thrust belt with a double vergence, resulting from the collision of the European and African continental margins between the Middle Cretaceous and the Late Eocene. The Po Plain is an alluvial region, resulting from marine (older) and fluvial (more recent) sed-

Table 1: Numerical values of the parameters used in STONE. “Class ID” and “Lithological Class” refer to the 19 classes identified in the geo–mechanical map of **Bucci et al. (2022)**. The parameter values shown here were used before in STONE by **Alvioli et al. (2021)**; the program performs random sampling of values of the parameters in a range around the nominal values, which we set to $\pm 10\%$.

Class ID	Lithological Class	Dynamic Friction	Normal Restitution	Tangential Restitution
L1	Anthropic deposits	0.65	35	55
L2	Alluvial, lacustrine, marine, eluvial, colluvial dep	0.80	15	40
L3	Coastal deposits, not related to fluvial processes	0.65	35	55
L4	Landslides	0.65	35	55
L5	Glacial deposits	0.65	35	55
L6	Loosely packed clastic deposits	0.35	45	55
L7	Consolidated clastic deposits	0.40	55	65
L8	Marls	0.40	55	65
L9	Carbonates-siliciclastic and marl sequence	0.35	60	70
L10	Chaotic rocks, mélange	0.35	45	55
L11	Flysch	0.40	55	65
L12	Carbonate Rocks	0.30	65	75
L13	Evaporites	0.35	45	55
L14	Pyroclastic rocks and ignimbrites	0.40	55	65
L15	Lava and basalts	0.30	65	75
L16	Intrusive igneous rocks	0.30	65	75
L17	Schists	0.35	60	70
L18	Non-schists	0.30	65	75
L19	Lakes, glaciers	0.95	10	10

imentation, between the the Southern Alps and Northern Apennines. The Apennines are the result of the collision of the western continental margin of the African Promontory with the Sardinia–Corsica block, which happened mainly during Miocene–Pliocene time, and consists of a series of east-verging areas. The Apennine chain can be subdivided into Northern Apennines and Central–Southern Apennines, bounded by regional transcurrent faults. Most of Sicily belongs to the northern continental margin of Africa, while Sardinia (with Corsica, France) is a fragment of the European continent. Additional details on the geology of Italy can be found in **Bosellini (2017)**, and references therein. A full geo–lithological map at 1:100,000 scale, the highest geographical scale for which a digital map is available for the whole of Italy, was recently obtained by **Bucci et al. (2022)** specifically for geo–mechanical modeling (used here). **Figure 2(b)** shows a full-size version of the thumbnail of the geo–lithological map in **Fig. 1(b)**; the lithological classes correspond with the ones listed in **Table 1**.

The remarkable extension of Italy in latitude result in diverse climatic conditions. The orography of the Apennines and the Alps substantially influence weather fronts, winds, and temperature distribution, exposing different areas of Italy to specific types of circulation (**Fратиани and Acquotta, 2017; Mazzoglio et al., 2021**). The Alps have a barrier effect from the cold currents from the North, while the Apennines limit the influence of moist air to the Tyrrhenian side along the entire peninsula, and protect

from the cold easterly winds that hit the Adriatic side during winter. The Mediterranean Sea has a mitigating effect on climate; the distribution of atmospheric pressure over the Peninsula and over the surrounding seas is one of the fundamental factors which affects the meteorological regimes. Due to these factors, the main climatic regions according to the Köppen classification falls entirely within the Mediterranean climate area, which belongs to a subtropical climate type with dry summers, with areas belonging to other meso-thermal climates and situations of micro-thermal or altitude climates. A full summary of climatic classification based on the Köppen–Geiger scheme, temperature and precipitation distribution in Italy is in **Fратиани and Acquotta (2017)**. They also argue that onset of climatic changes shows gradual increase in temperature and a change in the annual distribution of precipitation throughout the country (**Fратиани and Acquotta, 2017**). Projected climatic changes are expected to have an effect on slope stability, in terms of frequency and magnitude of landslide phenomena (see *e.g.*, **Alvioli et al. (2018)** and references therein).

The geology of Italy determines a substantial seismic hazard in many areas of the country. The INGV publishes seismic hazard maps, *i.e.*, maps of the expected seismic shaking due to an earthquake. **Figure 2(c)** shows a map of the expected maximum ground acceleration with exceeding probability of 10% in 50 years (**Stucchi et al., 2004**), in units of the acceleration of gravity, g . Largest values (larger than $0.225 g$) are expected in

Calabria, South–Eastern Sicily, Friuli–Venezia Giulia and throughout the Central–Southern Apennines. The figure also shows a point inventory of earthquake–induced landslides, known as CEDIT (Martino et al., 2014; Caprari et al., 2018). It contains a total of 2,058 points, classified as 16 different types of landslides. The vast majority are rockfalls (1,093), though 459 points are unclassified.

4 Methods

This section describes the framework adopted to obtain maps of seismically–induced rockfall hazard in Italy. These include: (i) a specific choice of mapping units, for the analysis of mapped rockfall sources and to aggregate results; (ii) a numerical model to simulate in three dimensions the trajectories of falling blocks; (iii) maps describing the expected seismic shaking with two different return times; (iv) a novel mechanism for localizing initiation points of trajectories, linking the seismic trigger to predisposing factors defined by local topography and different physiographic settings in Italy. The overall framework adopted in this work is summarized graphically in Fig. 1. We described each of these topics in separate sections, as follows.

4.1 Optimized slope unit delineation

Slope units are mapping units well suited for landslide studies, both with statistical (Tanyaş et al., 2019b; Pokharel et al., 2021) and with physically based approaches (Doménech et al., 2020; Alvioli et al., 2021; López-Vinielles et al., 2021; Marchesini et al., 2021; Alvioli et al., 2022a). They are polygons delimited by drainage and divide lines obtained solely from a specific DEM. The advantage of using slope units instead of the standard grid cells is their correspondence with the real landscape; a slope unit is a representation of a hill slope on a digital landscape. As such, one can assume with reasonable confidence that the likelihood of landslide occurrence within a given slope unit polygon is uniform. This gives a second, important advantage: inaccuracies or mismatches of input data for a specific model are mitigated by aggregation at slope unit level (Jacobs et al., 2020).

Drainage and divide lines for a specific DEM are not univocally determined. This is due to different existing methods and software to perform such delineation and, most importantly, to the required level of detail. That results in slope units of different sizes, due not only to differences in local terrain roughness but also to the choice of a scale for the analysis. This, in turn, is reflected in different parameters controlling the size of slope unit in dedicated software.

In this work, we adopted slope units obtained from the software `r.slopeunits` (Alvioli et al., 2016). Parameters controlling the scale of slope units delineation, in the

software, were optimized at the national level by Alvioli et al. (2020). Optimization was performed using only morphometric considerations, by maximizing the capacity of the polygonal map of segmenting a DEM with 25 m grid size¹ into mapping units with well–defined slope aspect. Details of the delineation and optimization procedure are given in the cited bibliography, for the interested reader; a thumbnail image showing the portion of Italy covered by the 300,000 slope unit polygons is in Fig. 1(d).

4.2 Simulation of rockfall trajectories with STONE

The numerical model used in this work, STONE, describes trajectories of falling blocks from their detachment point to their rest point downhill. In the model, a rockfall trajectory is a combination of three possible processes: free falling, bouncing and rolling. Each of them is controlled by mechanical laws described by simple equations, in the computer program. The code, however, does not contain a mechanism for the actual detachment of blocks. This is due to the limitation posed by the amount of knowledge required to model the detachment process: data about the conditions of the rocks, their fracturing pattern, weathering state, and others (Mavrouli and Corominas, 2020; Hendrickx et al., 2022; Núñez-Andrés et al., 2023). In addition, a specific description of the mechanism, like sliding, toppling or falling, would be required to link those conditions and local morphology of the rocks to an actual probability of detachment.

In this work, we deal with seismically–induced rockfalls. We devised a probabilistic procedure to define the locations of possible detachment points as a function of slope, and a selective triggering of the possible sources driven by seismic ground shaking. This allows producing a map of rockfall source locations (one of the main inputs of STONE) as a function of ground shaking scenarios and of local topography. Details of this process are in Section 4.4, and are original of this work.

The calculation of trajectories themselves, instead, is completely delegated to runs of the numerical code, initialized with a DEM map, the map of sources, and maps of local values of numerical coefficients controlling the different processes involved in the calculations. The latter consisted in three different coefficients: friction, controlling the behavior of blocks during rolling, and normal and tangential restitution, controlling energy loss during bouncing impacts on the ground. Table 1 shows numerical values of the coefficients, for different lithological classes at 1:100,000 scale (Bucci et al., 2022), adopted both in Alvioli et al. (2021) and here.

The model STONE describes falling blocks as point–like,

¹The resolution of the DEM used to prepare slope units, 25 m, is smaller than the resolution of the DEM used here for simulations; this does not affect results in any way, as slope units are only used to aggregate final results.

Table 2: The different physiographic provinces (rows in bold) and sections of **Guzzetti and Reichenbach (1994)**, modified as in **Alvioli et al. (2021)**. The table shows the parameters a and b appearing in **Eq. (3)** and controlling the probability of having static rockfall sources $P_{static}(S)$ as a function of slope, S . The areal extent of each topographic unit, its percent surface and area covered by slope units (SU) are also listed. See **Fig. 2** for map of the geographical distribution of the physiographic provinces and sections.

Province/Section	a	b	Extent [km ²]	Percent	SU Area [km ²]
1.: Alpine Mountain System	–	–	52,010	17.4	51,739
1.1: Western Alps	0.11	5.54	16,274	5.4	16,547
1.2 & 1.3: Central-Eastern Alps & Carso	0.13	4.32	35,735	11.9	35,191
2.: North Italian Plain	–	–	46,531	15.54	4,580
2.1: Po Plain	0.21	6.86	32,702	10.9	1,694
2.2: Veneto Plain	0.11	13.00	9,426	3.2	550
2.3a: North-Western Alpine Foothills	0.11	8.59	3,103	1.0	1,950
2.3b: South-Western Alpine Foothills	0.31	4.30	1,298	0.4	359
3.: Alpine–Apennines Transition Zone	–	–	6,313	2.1	6,117
3.1: Monferrato Hills	0.11	2.92	2,322	0.8	1,918
3.2: Ligurian Upland	0.11	5.71	3,991	1.3	4,199
4.: Apennine Mountain System	–	–	80,947	27.0	82,179
4.1: Northern Apennines	0.11	6.78	22,393	7.5	23,886
4.2: Central Apennines	0.11	6.41	16,835	5.6	17,386
4.3: Molise Apennines	0.11	9.70	4,920	1.6	5,136
4.4: Molise-Lucanian Hills	0.11	9.64	8,097	2.7	8,345
4.5: Lucanian Apennines	0.15	7.06	12,890	4.3	12,651
4.6: Sila	0.11	8.31	6,203	2.1	5,638
4.7: Aspromonte	0.11	5.98	5,337	1.8	4,959
4.8: Sicilian Apennines	0.11	6.39	4,262	1.4	4,176
5.: Tyrrhenian Borderland	–	–	37,857	12.64	29,404
5.1: Central Italian Hills	0.11	8.32	25,346	8.5	20,022
5.2: Tosco-Laziale Section	0.17	2.92	6,136	2.0	5,181
5.3: Lazio-Campanian Section	0.11	7.43	6,375	2.1	4,201
6.: Adriatic Borderland	–	–	31,062	10.35	17,521
6.1: Central Apennine Slope	0.11	5.41	9,023	3.0	8,230
6.2: Murge-Apulia Lowland	0.11	36.77	20,236	6.8	7,923
6.3: Gargano Upland	0.11	3.00	1,731	0.6	1,368
7.: Sicily	–	–	21,105	7.1	18,867
7.1 & 7.2: Marsala Lowland & Sicilian Hills	0.11	14.72	14,285	4.8	13,273
7.3: Iblei Plateau	0.11	11.81	5,321	1.8	4,178
7.4: Etna	0.17	19.10	1,499	0.5	1,416
8.: Sardinia	–	–	23,790	7.9	19,320
8.1: Sardinian Hills	0.11	19.57	16,404	5.5	14,548
8.2: Gennargentu Highland	0.11	6.50	2,580	0.9	2,209
8.3: Campidano Plain	0.11	23.22	1,946	0.6	190
8.4: Iglesiente Hills	0.11	23.20	2,844	0.9	2,375

and neglects air drag, as their velocity is usually not large enough to make it relevant. The code considers each grid cell selected as a rockfall source and calculates the trajectory followed by the block until it comes to a rest. The trajectory depends on the topography and on the coefficients

controlling the loss of velocity during bouncing and rolling. The topography is described using a terrain regular network of triangles, built on the equally spaced elevation points of the input DEM. The simulation is not fully dynamical, in that the code does not consider the shape

and mass of blocks; this makes the simulation fast, and we can simulate hundreds of different trajectories for each source cell. In fact the code contains a certain degree of randomization involving the detachment angle and terrain coefficients, which makes trajectories simulated from the same source point slightly different from each other. The degree of variability is selected by the user, and it usually ranges between $\pm 5\%$ and $\pm 10\%$ around central values in **Table 2**, for the coefficients, and around the horizontal direction, for the angle of detachment.

In the code, the possibility for the blocks to break apart into smaller fragments (Matas et al., 2017; Núñez-Andrés et al., 2022) is not accounted for. An assessment of the effects of these approximation is beyond the scope of this work, and will be addressed elsewhere. Nevertheless, we believe that in the present context of a national-scale application of the code, the approximations are largely justified – mostly because the major role, here, is played by the triggering mechanism of rockfalls.

Output of the computer program is rockfall count, a raster map whose values represent the number of intersections of rockfall trajectories with the local topography, in each grid cell. The output assumes a probabilistic meaning, because (i) the code contains random variations of input parameters drawn from probability distributions at each simulation, and (ii) from each source location it simulates many possible trajectories, which are all different in virtue of the randomness in the code. Thus, the count in one particular location represents the relative probability of that particular grid cell of being hit, for given sources and conditions set by the user.

4.3 Scenarios for peak ground acceleration

We adopted PGA maps obtained as in Falcone et al. (2021) and Mendicelli et al. (2022), for two different return times, which we considered as different rockfall-triggering scenarios. Previous works obtained the ratio between expected ground motion at the site of interest and that at the outcropping engineering bedrock, known as amplification factor (AF). The morpho-geological clusters proposed by Iwahashi et al. (2018) were adopted to generate specific AF- V_{S30} correlations. In fact, morpho-geological properties (*i.e.*, normalized slope, local convexity, and surface texture) provide useful criteria to recognize homogeneous area for dynamic purposes (Mori et al., 2020; Falcone et al., 2021). The polygons were useful to group the 11,300 V_{S30} values and the subsoil lithologies groups of the 35,000 borehole data logs. Additional input data for the purpose are listed in **Section 3.1**.

Seismic site response analyses were performed using the NC92Soil code (Falcone et al., 2021), based on the equivalent linear approach in the frequency domain. The same code was adopted for the pre-processing of site data and post-processing of seismic site response analyses. The

software NC92Soil is a stand-alone Windows application written in Python. At its core is the well-known code Strata (pystrata) for the analysis of local seismic response (Kottke et al., 2013). NC92Soil works with a graphical user interface, to run multiple parametric analyses for professional and research activities. Inputs of the software are underground profiles, time series and response spectra; it performs equivalent linear site response analysis in the frequency domain, using time domain input motions or random vibration theory methods, and can perform both deterministic and stochastic analysis of the site properties.

PGA maps at the level of outcropping flat bedrock, PGA_{rock} , were retrieved from the seismic hazard study provided by the INGV (Meletti and Montaldo, 2007; Montaldo and Meletti, 2007) considering the median values. Out of the nine return times available from INGV, we selected 475 y for this is the typical return time considered in Italy to assess effects on residential buildings, used in seismic microzonation studies. We also selected 975 y to illustrate the possibility of including different return times in the newly proposed framework.

Recurrent site conditions were defined according to seismic microzonation studies (Benigni et al., 2018). Using such data, Falcone et al. (2021) performed a set of about 30 million numerical simulations of local seismic site response, adopting an equivalent linear approach in the frequency domain. A total of 378 AF- V_{S30} relations were obtained, using the following expression:

$$\ln(AF) = a [\ln(V_{S30})]^2 + b \ln(V_{S30}) + c, \quad (1)$$

where the parameters a , b , and c depend on the intensity of the input ground motion, the geomorphological cluster, and percentile of interest (16^{th} , 50^{th} , and 84^{th}). Maps of

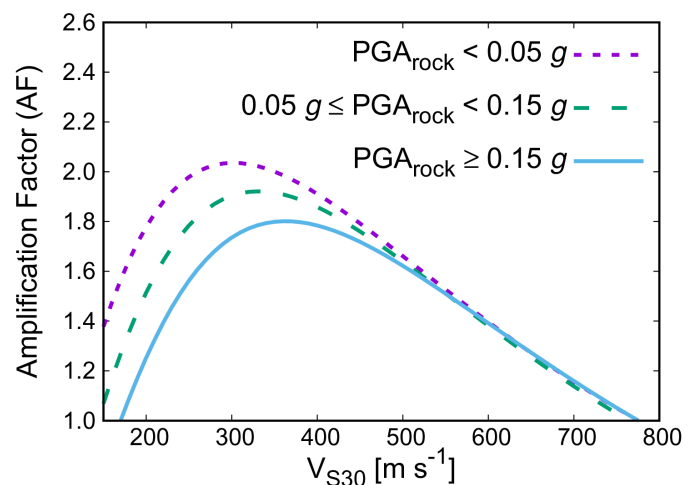


Figure 3: The AF- V_{S30} correlation, **Eq. (1)**, corresponding to the 50th percentile. PGA_{rock} is the reference ground motion at the ideal flat outcropping rock. The correlation is illustrated for one of the 42 considered morpho-geological clusters.

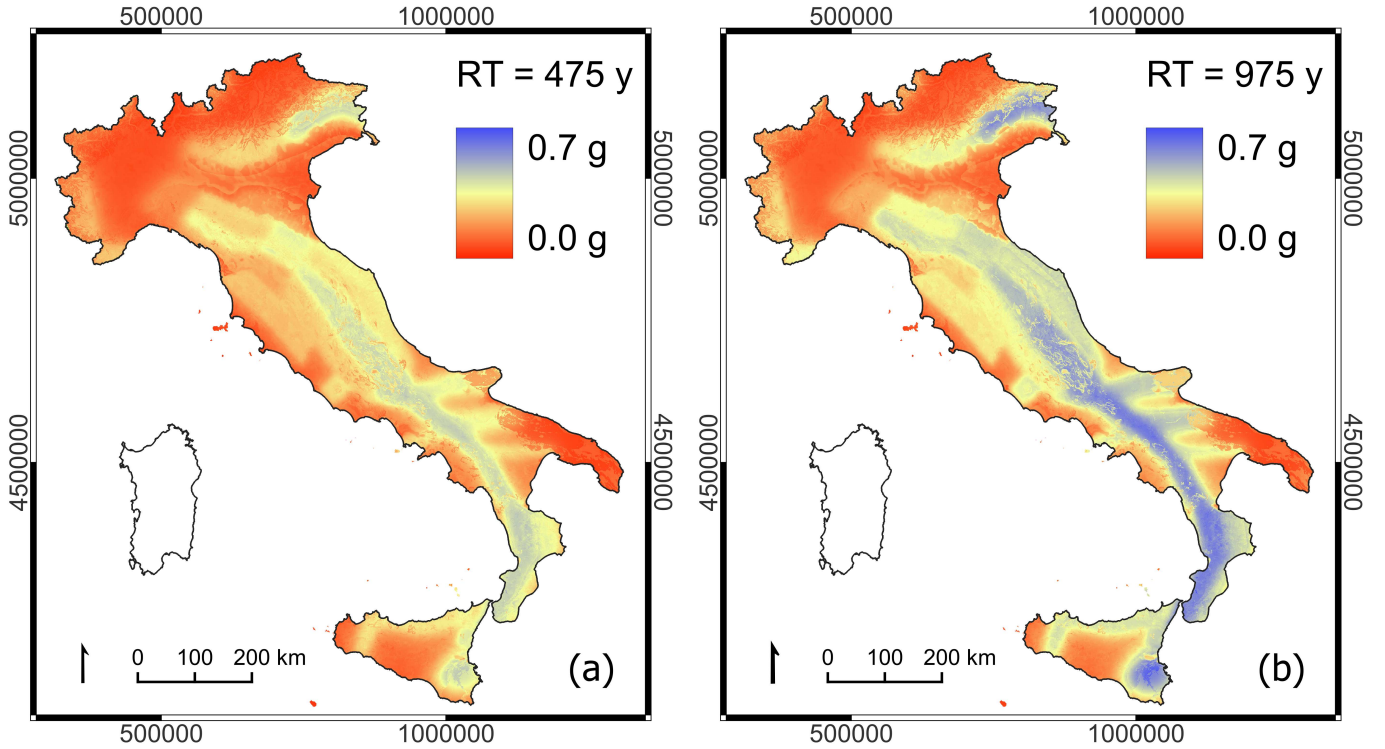


Figure 4: The PGA maps corresponding to 475 y return time (a) and to 975 y return time (b) scenarios, in units of g – the acceleration of gravity. In both cases, the figures show values of PGA corresponding to the 50th percentile of the procedure described in **Section 4.3**. In this work, we also used values corresponding to the percentiles 16th and 84th (not shown here) to calculate uncertainty on the final rockfall hazard maps, for both return times.

amplification factors were aligned to a 50 m x 50 m grid consistent with the V_{S30} map by **Mori et al. (2020)**. **Figure 3** shows an example of AF– V_{S30} correlation, corresponding to one of the 42 morpho–geological clusters. The AF– V_{S30} relation is non–linear, it depends on V_{S30} and on PGA_{rock} , *i.e.*, the reference ground motion at the ideal flat outcropping rock which depends on the site of interest and on the considered return period.

It is worth noting that PGA_{rock} is provided by INGV for a 5 km x 5 km grid; hence, PGA_{rock} for a 50 m x 50 m grid can be obtained by interpolating INGV data. Hence, the amplified ground shaking was obtained as the product of the PGA_{rock} and the AF maps. For sake of brevity, the amplified PGA is herein named PGA_{RT}^p where p is the percentile, $p \in \{16, 50, 84\}$, and the RT is the return time, $RT \in \{475, 975\}$. The PGA maps considered here are new to this work and were calculated for the specific purpose of inferring rockfall hazard; previous work only illustrated AF maps, and only for the 475 y return time.

We are aware that slope seismic response (**Bouckovalas and Papadimitriou, 2005; Massey et al., 2017**) is generally more complex than the one–dimensional ground motion studied by **Falcone et al. (2021)**. Furthermore, it is difficult to provide AF based on multi–dimensional schemes and numerical simulation of seismic site response for the entire Italian territory. Hence, AF considers the

sole sub–soil setting in this study, and improvements to include AF based on more complex numerical approaches will be presented elsewhere. Moreover, bearing in mind that topographic and stratigraphic amplifications (**Assimaki et al., 2005**) are in the range 1.0–1.4 and 1.0–4.0, respectively, we decided to consider the only ground shaking modification induced by the geo–lithological condition.

Figure 4 shows PGA maps corresponding to 475 y return time and 975 y return time scenarios. In both cases, the figures show values corresponding to the 50th percentile of the procedure described in this section. In this work, we also used values corresponding to the percentiles 16th and 84th to calculate uncertainty on the final rockfall hazard maps, for both return times, as explained in the next section.

4.4 Seismic triggering of rockfall sources

The main novelty introduced in this work is a mechanism to combine information from static, time– and trigger–independent potential rockfall sources, with scenarios for peak ground acceleration due to seismic shaking. This allows devising probabilistic maps of seismically–induced rockfall sources, linked to a given return time, corresponding to the return time associated with the selected PGA

scenarios.

The general idea behind the method introduced here is the intuitive assumption that an earthquake hitting a rockfall-prone area would trigger a larger number of landslides in locations experiencing larger values of PGA, relative to areas with smaller PGA values (**Valagussa et al., 2019; Massey et al., 2014**). This idea is implemented, here, by (i) adopting a static map of potential rockfall sources, solely obtained from data-driven morphometric considerations, which identifies rockfall-prone areas, and (ii) using a well-defined function of PGA values to selectively activate static sources, with probability dictated by the magnitude of a PGA map. The method can be summarized in a simple way by defining a triggering probability as a function of slope angle S and PGA , as follows:

$$P_{trigger}(S, PGA) = P_{static}(S) F_{RT}(PGA), \quad (2)$$

where $P_{static}(S)$ denotes the probability of a grid cell of being a rockfall source as a function of slope (*i.e.*, the source map developed by **Alvioli et al. (2021)** and extended here to the whole of Italy), and $F_{RT}(PGA)$ is an increasing, monotonic function of PGA values, such that $0 \leq F_{RT}(PGA) \leq 1$, and RT denotes a specific choice of return time.

The $P_{static}(S)$ map is defined as follows:

$$P_{static}(S) = \begin{cases} 0 & S \leq a, \\ b (S/90)^4 & S > a, \end{cases} \quad (3)$$

where the parameters a and b were obtained from sample source areas mapped by expert geomorphologists, as described in **Alvioli et al. (2021)**.

The procedure makes use a relatively small set of observation to infer a probability as a function of slope with a small number of parameters (**Eq. (3)**). **Alvioli et al. (2021)** carefully selected representative locations, and mapped polygons of potential rockfall sources in an expert way. They took care in surveying the whole slope unit containing the representative locations. This allowed to estimate the probability of sources as a function of slope, by taking the ratio of the distribution of slope values within the mapped polygons to the distribution of slope values within the whole slope unit. The collection of such ratios for many slope units allows obtaining the parameters in (**Eq. 3**) by quantile regression.

The parameter values were obtained independently for each of the physiographic units originally defined by **Guzzetti and Reichenbach (1994)** and further modified by **Alvioli et al. (2021)**. The total number of mapped source polygons to perform the quantile regression was 2,644 (a small sample is in **Fig. 1(c)**), and the calibration procedure was performed separately in 637 slope units. The numerical values of the parameter b in **Eq. (3)**, for each physiographic unit, are listed in **Table 2**; the units themselves are shown in **Fig. 1(a)**.

We adopted the simplest possible choice to map PGA values into the $[0,1]$ interval, namely:

$$F_{RT}(PGA) = \frac{PGA_{RT} - PGA_{min}}{PGA_{max} - PGA_{min}}. \quad (4)$$

Calculation of the function in **Eq. (4)** requires careful considerations, though. In fact, in this work we are interested in assessing the effect of two different PGA maps; both maps are national (except for the Sardinia Island, which has negligible seismic hazard; *cf.* **Fig. 4**), and they refer to two different return times, providing two different scenarios. Thus, triggering of static sources $F_{static}(S)$ must be consistent across the two PGA maps.

To this end, the values PGA_{min} and PGA_{max} in **Eq. (4)** must cover the whole range of PGA values in both maps; again, the simplest choice is to set $PGA_{min} = 0$ and $PGA_{max} = 0.81$ (in percents of g , the acceleration of gravity); the first value is actually the minimum of the PGA_{475} map, and the second value is actually the maximum of the PGA_{975} map, not surprisingly. Then, **Eq. (4)** tells us that $F(PGA)$ is a linear mapping of $[0,0.81]$ into $[0,1]$; insertion of such function in **Eq. (2)** gives the final map of seismically induced rockfall sources, as a function of slope and PGA, where the latter is either from PGA_{475} or PGA_{975} . The two maps resulting from $P_{trigger}(S, PGA_{475,975})$ are the main input of the program STONE for the simulation of rockfall trajectories corresponding to the two seismic shaking scenarios.

Actually, the procedure for the calculation of ground shaking maps described in **Section 4.3** is a probabilistic one, and as such it produces PGA maps for a given probability, for a given return time RT. For this work we decided to consider three maps for each RT scenario; one, corresponding to the 50th percentile, PGA_{RT}^{50} , which we considered as the main triggering PGA map; two additional maps, corresponding to the 16th and 84th percentiles, PGA_{RT}^{16} and PGA_{RT}^{84} , which we used to calculate the uncertainty of the central value. In conclusion, we performed three production runs for each considered return time.

5 Results

Results of simulations with STONE are summarized in **Fig. 5**, at national scale, and **Figs. 6-8**, which show details in three different areas in North-Eastern, Central, and Southern Italy, respectively. The four panels in each figure show results for both the return times considered in this work, 475 y and 975 y. The left panels show results corresponding to simulations with rockfall sources triggered with the 50th percentile of PGA maps; the right panels show uncertainties related to each map, calculated using information (the difference) from simulations with sources corresponding to the 16th and 84th percentiles. Both results are aggregated at slope unit level, and classified in five categories as follows.

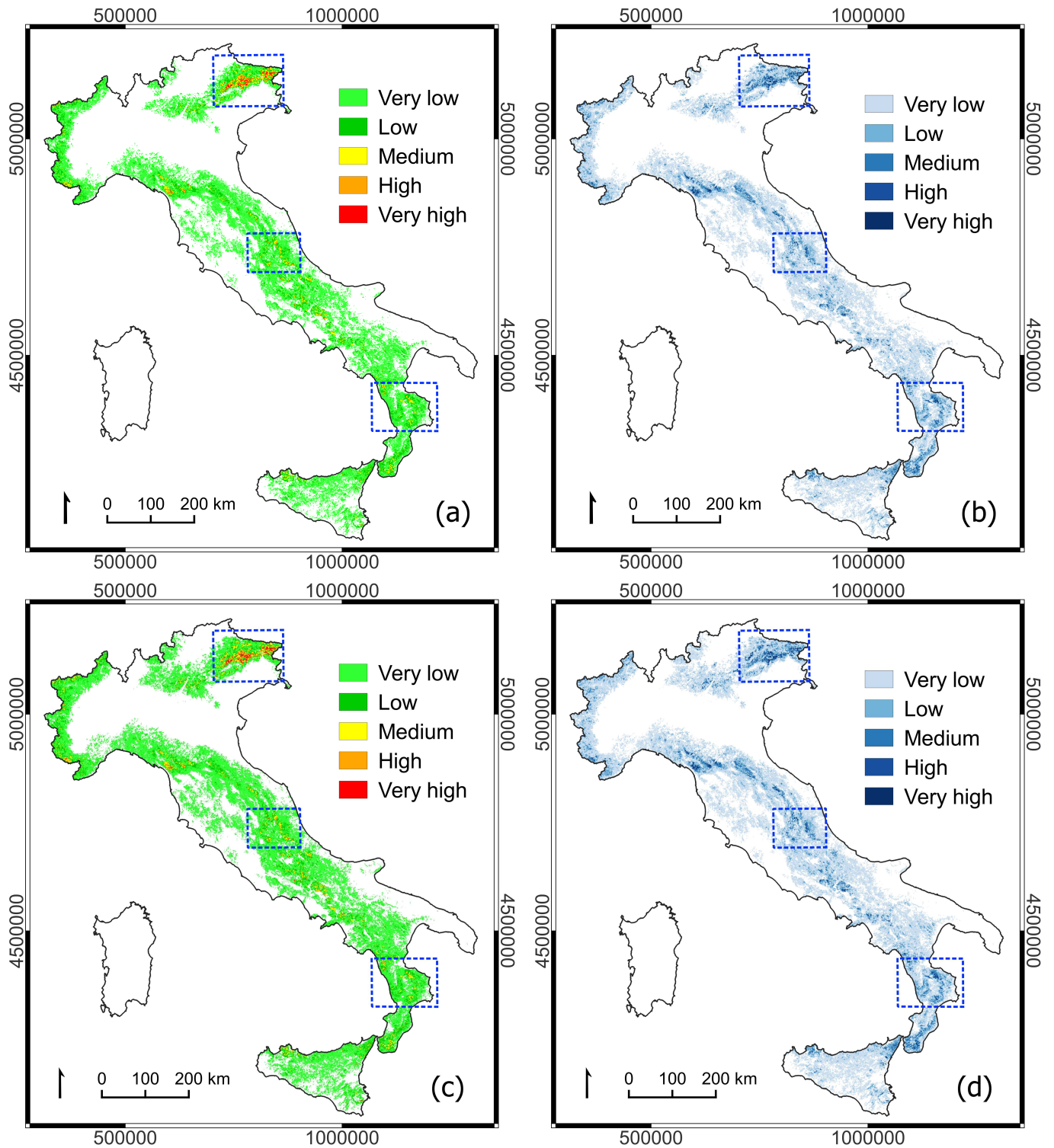


Figure 5: Results of rockfall simulations for input PGA map corresponding to 475 y return time (top row) and to 975 y return time (bottom row). Left: number of trajectories per pixel obtained with the PGA map at 50th percentile, averaged within individual slope units and classified in five categories. Right: uncertainty on the left result, calculated as the difference of the results corresponding to the 84th and the 16th percentiles in each slope unit; the difference was classified in five categories. Maps in WGS84/UTM32, EPSG:32632.

The main output of the program STONE is a raster map with trajectory count in each grid cell. We first noted that about one third out of the 325,578 slope units had null values (111,219 for 475 y and 129,149 for 975 y), meaning that

no trajectories at all were present in the corresponding polygons. We considered those slope units equivalent to flat areas, in which earthquake-induced rockfalls may not occur, and disregarded them in the classification. Next, we aggregated non-null records of the raw output at slope unit level, by assigning the average count to each slope unit; eventually, we classified the results using a head/tail breaks method. We opted for this classification method for the distribution of average values is very skewed towards zero (*cf.* **Figure 9(a)**), and equal-interval or quantile classification is not effective, in such cases.

On the other hand, head/tail classification is well suited for unbalanced distribution where the average value splits the original set into two subsets containing about 20% and 80% of the original values. The most numerous subset is taken as a final class, while the less numerous set is split further using the mean as a break. The process is iterated until one gets five classes. In our case, we obtained the break values listed in **Table 3**, separately for the two return times. The table also lists the number of slope units in each class, and the total area covered by them. Classes are denoted as very low (VL), low (Lo), medium (Me), high (Hi), and very high (VH), referring to the likelihood of a rockfall occurring in the corresponding slope unit.

Uncertainty maps in **Figs. 5-8** were obtained as the difference of the results of STONE initialized with source maps corresponding the 84th and 16th percentiles of PGA maps. In this case the distribution of values (*cf.* **Figure 9(b)**) has negative and positive values, thus we considered as uncertainty the absolute value of the difference. Negative values were much less than the positive values, consistently with the definition of uncertainty adopted here: we expect the results from 84th percentile to be numerically larger than the results from the 16th percentile. Moreover, it is worth noting that the higher the ground shaking intensity the lower the amplification factor, as shown in **Fig. 3**. As a consequence, the uncertainty maps are expected to provide negative values in such rare cases of steep slope and soft material (*i.e.*, $V_{S30} \leq 650$ m/s). In conclusion, we applied the head/tail breaks method to the absolute value of the difference and **Table 4** shows, separately for the two return times, the number of slope units in each class, and the total area covered by them.

Figure 10 shows a comparison between the rockfall count result and the slope unit average, in a selected location, for the shortest return time, RT=475 y. The figure shows four different zoom levels in the same location; for each zoom level, we show on the left the results of the slope unit-based average procedure, and on the right the corresponding rockfall count map. The latter was classified in five categories, using the head/tail method as in the case of averaged values, with the same meaning (VL, Lo, Me, Hi, VH). This figure illustrates the procedure of aggregation at slope unit level, and gives an idea of the actual resolution of simulations, applied consistently all over Italy.

Eventually, we performed a consistency check of results with 475 y return time. In fact, we wanted to make sure that results of simulations with STONE, aggregation and classification of the map corresponding to PGA_{475}^{50} were not trivial results. In fact, it is straightforward that any slope stability issue is related to local slope angle, to some degree. Moreover, our model for static rockfall sources only considered slope angle as morphometric input. Thus analyzing the degree of correlation between the final result and slope values looks like a meaningful consistency check.

With a similar rationale, we checked the distribution of results for rockfall count as a function of the average value of peak ground acceleration, at slope unit level. This is also a relevant consistency check, because results with a trivial relationship between rockfall count and PGA would not be a robust result, and would suggest that the seismic forcing would be the most relevant ingredient of the modeling chain – regardless of all other inputs, including the “static” source map $P_{static}(S)$.

To this end, we prepared a scatter plot of susceptibility values, prior to classification, as a function of slope values, considering both values of rockfall trajectory count, slope, and PGA, all aggregated at slope unit level. **Figure 11** shows the results of this check; **Figure 11(a)** shows the rockfall count *vs.* slope scatter plot, while **Figure 11(b)** shows rockfall count *vs.* PGA. In both figures, each dot correspond to an individual slope unit (with non-null value of average rockfall count, *i.e.*, 111,219 units out of 325,578), and the colors of the dots match those of the uncertainty associated to susceptibility values, as shown in **Fig. 5** (RT = 475 y).

Figure 13 show a comparison of model results, *i.e.*, the maps of **Fig. 5** for RT=475 y and RT=975 y, and the CEDIT point inventory of seismically-induced landslides. Even if the model adopted in this work can only describe rockfalls, we compared separately the model results with observed rockfalls and other kinds of landslides, to highlight differences. Landslides in the inventory do not bear information about the triggering earthquake event (nor other competing parameters, like antecedent rainfall, for example), thus we compared data with results from both values of RT. We calculated the percentage of SU falling in each class, in the results, and the percentage of landslides falling within SU, in each class. We did not consider points falling in areas predicted as null by the model, which were not negligible (about 5% for rockfalls).

The figure shows that, for rockfalls (**Fig. 13(a)-(c)**), percentages for actual data exceeds those from the model, in intermediate and higher classes, while it is always less than the model, in the lowest class. As that is true for both values of RT (actually the signal is larger for RT=975 y), this means that the points corresponding to rockfalls are not randomly distributed, but they fall preferentially in higher-hazard than smaller-hazard classes. It is also use-

Table 3: Classification of results corresponding to rockfall sources triggered by the PGA_{RT}^{50} maps, for both return times of 475 y and 975 y (*cf.* **Section 4.3**). Classification was performed using the head/tail breaks method. Maps are shown in **Fig. 5** (national) and **Figs. 6-8** (details).

475 y	Class	Percentage after break	Breaks	No. Records	Total area [km ²]
	1	81%	< 10.2	89,761	86,154
	2	72%	10.2–45.4	15,485	14,712
	3	68%	45.4–106.9	4,082	4,029
	4	68%	106.9–190.8	1,295	1,282
	5	65%	> 190.8	596	570
Sum				111,219	106,747
975 y	Class	Percentage after break	Breaks	No. Records	Total area [km ²]
	1	80%	< 15.1	103,645	96,732
	2	72%	15.1–65.6	18,271	17,288
	3	68%	65.5–150.8	4,954	4,962
	4	67%	150.8–267.1	1,533	1,539
	5	65%	> 267.1	746	739
Sum				129,149	121,260

Table 4: Classification of uncertainty maps, calculated as the absolute value of the difference between the results of STONE obtained from $PGA_{RT}^{16,84}$ maps. Classification was performed using the head/tail method. Maps are shown in **Fig. 5** (national) and **Figs. 6-8** (details).

475 y	Class	Percentage after break	Breaks	No. Records	Total area [km ²]
	1	75%	< 2.44	83,831	84,018
	2	69%	2.44–8.10	18,762	15,970
	3	67%	8.10–15.97	5,812	4,705
	4	67%	15.97–25.74	1,880	1,401
	5	68%	> 25.74	934	654
Sum				111,219	106,747
975 y	Class	Percentage after break	Breaks	No. Records	Total area [km ²]
	1	75%	< 3.25	96,612	94,337
	2	68%	3.25–10.58	22,193	18,817
	3	67%	10.58–20.58	6,895	5,544
	4	68%	20.58–32.66	2,339	1,764
	5	70%	> 32.66	776	798
Sum				129,149	121,260

ful to look at non-rockfall points, **Fig. 13(b)-(d)**: in this case the percentages for data show almost the same distributions as the model results, indicating a lower agreement – as one should expect. The conclusions from **Fig. 13** are mostly qualitative, but we deem the conclusions we drew sufficient as a validation, given the available information. Results may also depend on the type of aggregation process used here (SU average; taking the largest value would be another viable option) and the classification of raster counts with the head/tail method.

The results of this work were included in a WebGIS application prepared to share with the public the results of the project funding this research (see **Section 9**). The

web interface aimed at characterizing seismically-induced rockfall hazard in Italy, within so-called *zone d’allerta* – a particular zonation adopted by the Italian Civil Protection to issue geo-hydrological alerts. As such, the system includes a wealth of information on the subject, ranging from basic cartography about seismology, landslide inventories, and geo-lithological properties, and more elaborate products, including a seismically-induced landslide probability map prepared with the method of (**Nowicki Jessee et al., 2018**) and the rockfall hazard maps proposed in this work. Details about accessibility of the WebGIS are in **Section 8**.

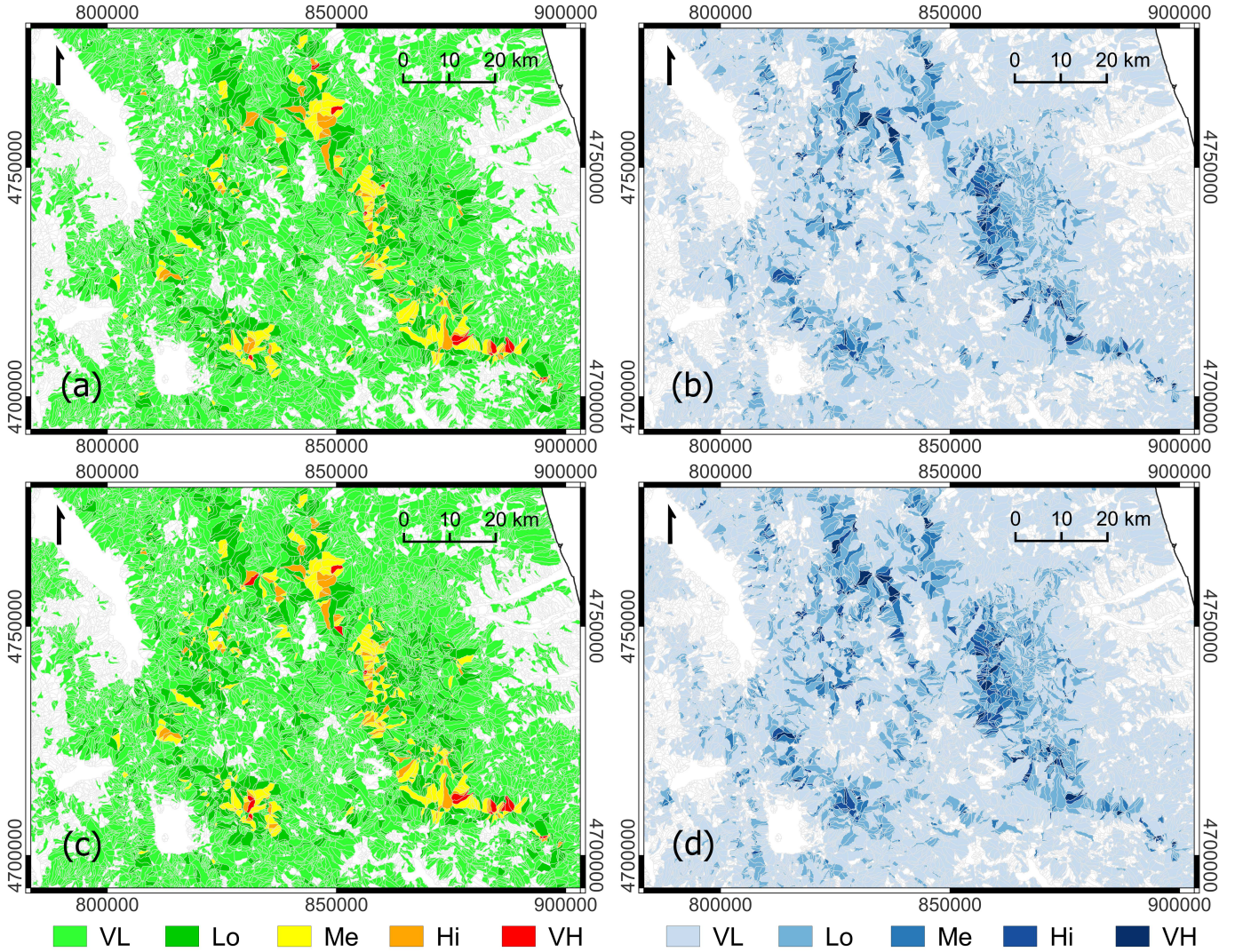


Figure 6: Details of the maps in **Fig. 5**, within the blue rectangle in Central Italy in the four maps.

6 Discussion

We first would like to comment on **Fig. 10** showing slope units averages *vs.* rockfall count at grid cell level. The figure has illustrative purposes and it allows appreciating the detail of the rockfall count maps produced by STONE in output. The latter has 10 m resolution, as the TINITALY DEM used in this work does. Each trajectory appears as 10 m wide because of the resolution, even if in the code they are calculated as curves in three-dimensional space, and DEM resolution is exploited to a maximum by introducing an additional triangulation of the topography. The maps in the right column of the figure, (b), (d), (f), and (h), show the superposition (total count, cell by cell) of trajectories, and a few of them can be resolved individually, despite the classification, especially at the largest zoom level, **Fig. 10(h)**. We stress that this is the level of detail applied throughout Italy, which is unique to our framework for physically based models (**Alvioli et al., 2021; Marchesini et al., 2021**). Aggregation at slope

unit level, on the other hand, was also used within other approaches with statistical methods, *e.g.* in **Amato et al. (2021)** and in **Loche et al. (2022a)**. The latter is dictated by the need of a mapping unit consistent with a national-scale interpretation of the results, while the native output of our simulation has much higher resolution – even if it does not imply higher accuracy.

Results in **Fig. 5** (national) and **Figs. 6-8** (details) show that the main difference between 475 y and 975 y return times is mostly in term of extent of the area in which hazard is not null. This is consistent with our formulation for the localization of seismically-induced rockfall source areas. In fact, the definition of **Eq. (2)** clearly shows that the probability of triggering a rockfall trajectory from a grid cell characterized by slope S and peak ground acceleration PGA is the product of two factors: a morphometric factor, $P_{static}(S)$, and a dynamic factor, $F_{RT}(PGA)$. The former only depends on slope, and thus it is common to the two different return times. Given that the the set of “static” sources which can potentially be activated is

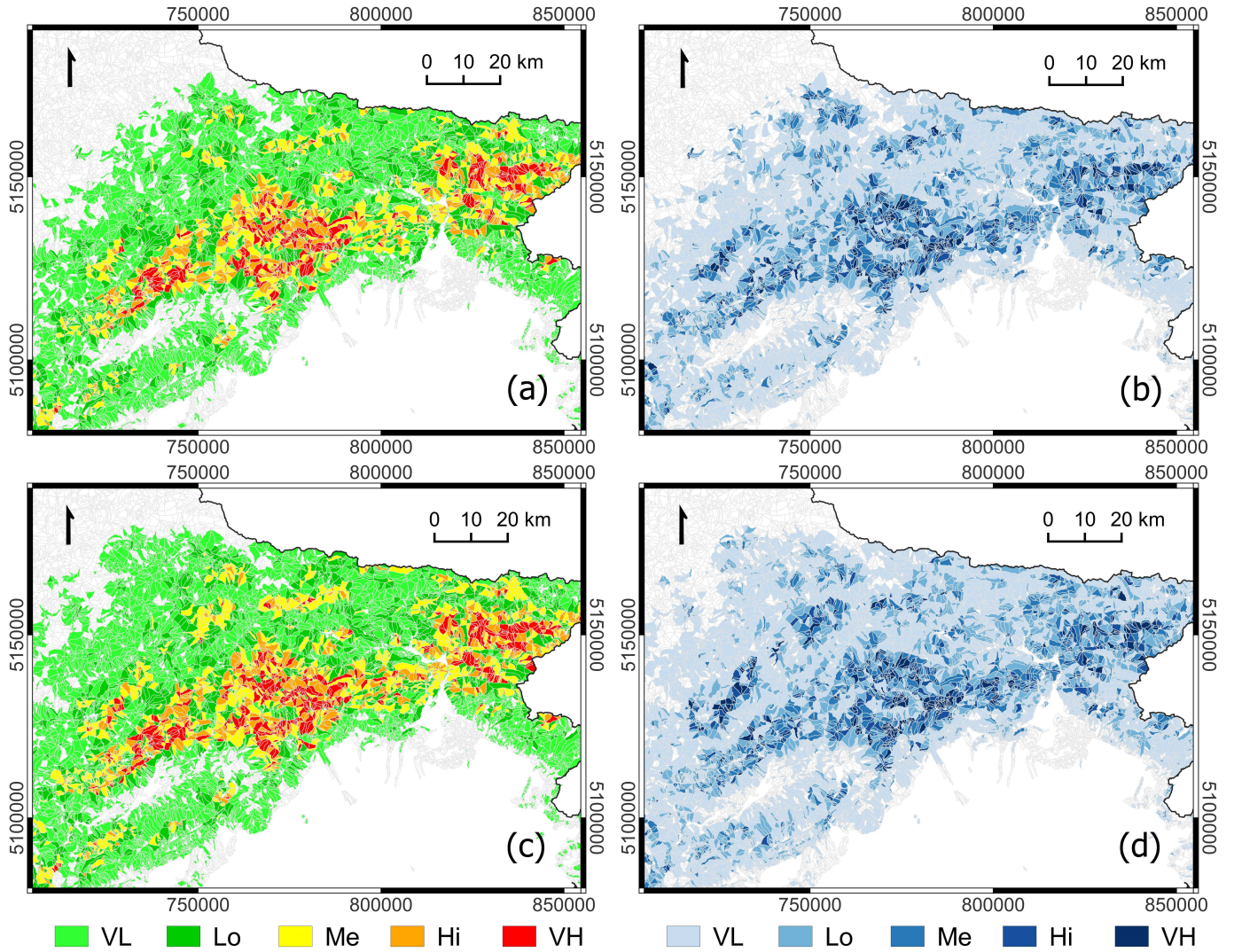


Figure 7: Details of the maps in **Fig. 5**, within the blue rectangle in North–Eastern Italy in the four maps.

common to either RT cases, in virtue of **Eq. (4)** and the spatial distribution of PGA_{RT} values of **Fig. 4** we can understand the behavior observed in the results.

Figures 5-8 show an assessment of uncertainty, besides the main results for hazard maps. Visual inspection is enough to realize that larger uncertainties are associated with higher values of hazard. To investigate this point quantitatively, **Figure 11** shows the relationship between the trajectory count and uncertainty, both averaged at slope unit level, for the two different return times considered here. Each slope unit corresponds to one dot; colors of the dots correspond to the classification explained in detail in **Table 3** and used in **Figs. 5-8**; horizontal dotted lines, instead, correspond to the classification of uncertainty values, explained in detail in **Table 4** and used in the same figures quoted above.

The general trend shown in **Figure 11** exhibits a clear power-law dependence of uncertainty upon trajectory count values. Power laws are ubiquitous and appearance

of one such (approximate) dependence, here, is not surprising. We conclude from this consistency check that uncertainty values are strongly correlated with average trajectory count – and the dependence is not linear, but exponential (linear in a log–log scatter plot), making reduction of uncertainty a priority for future work. A closer inspection of the figure reveals that most of the rockfall count values in the VL (very low, light green) class falls in the VL or Lo (low) classes in uncertainty, while all of the higher classes (Lo, low; Me, medium; Hi, high; VH, very high) are scattered over all classes of uncertainties. Thus, we conclude that for both return times, slope units with small rockfall count have a substantially more robust characterization of rockfall hazard.

Fig. 12 shows scatter plots of trajectory count *vs.* slope angle, in (a), and *vs.* peak ground acceleration in units of g , in (b). As in **Fig. 11**, each dot represents average values within a single slope unit but, in this case, colors correspond to the classes shown in **Table 4** for uncertainty, and horizontal dotted lines correspond to the classes shown in

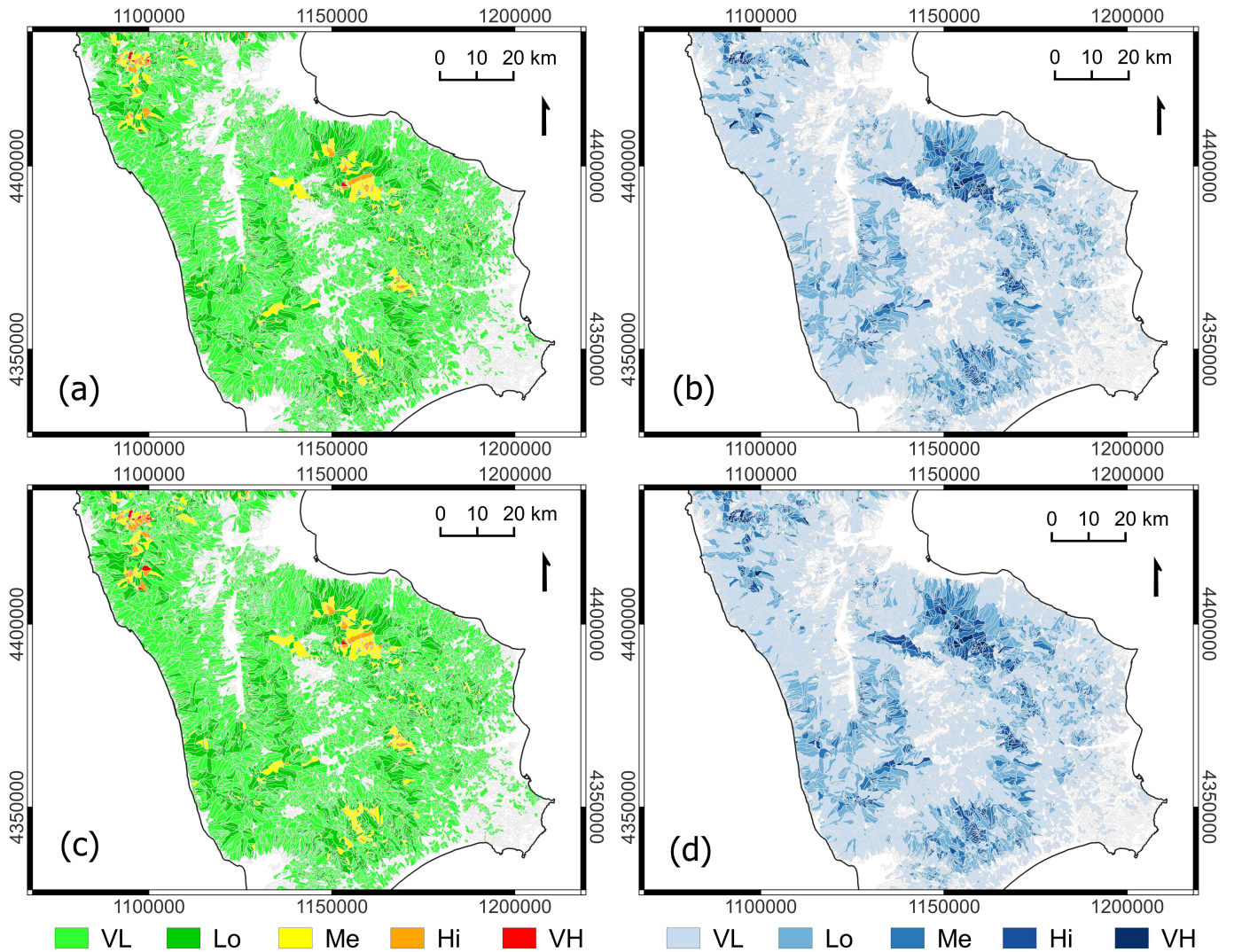


Figure 8: Details of the maps in Fig. 5, within the blue rectangle in Southern Italy in the four maps.

Table 3 for rockfall counts. At variance with the previous figure, the dependence on both slope and PGA values is absolutely not obvious, and values of rockfall counts are scattered with complex patterns both as a function of slope, in (a), and a function of PGA values, in (b).

We conclude, from this consistency check, that no obvious correlation exists between average trajectory count and average slope angle (we checked that the same holds for elevation, not shown here) and PGA values. In the latter a few dots appear to artificially align in the vertical direction but they represent a negligible minority within the whole sample. In general, for each interval of the trajectory count variable selected by the five classes, one can see that values of slope and PGA span over almost the whole existing range. Results show that both $P_{static}(S)$ and $F_{RT}(PGA)$ (cf. Eq. (2)) are relevant ingredients of the modeling chain and their contributions cannot be disentangled within the results in a trivial way.

Eventually, we would like to comment on the significance

of our results, on more general terms. We have shown that a physically based model is suitable for application on the large scale, and can provide alternative estimates of landslide (rockfall) susceptibility with respect to the statistical/machine learning approaches, widely used in the literature for large areas (Amato et al., 2021; Loche et al., 2022a; Wang et al., 2022). In fact, we have set up a computing and conceptual framework capable of running three-dimensional simulations within the program STONE, at high resolution, for the whole of Italy. Results of the model are readily interpreted as spatial likelihood of rockfall occurrence. There are multiple advantages in adopting a physically based assessment, instead of a statistical one, which is the traditional approach for large areas.

First, with the former, one obtains a high-resolution output, which can be utilized in different ways depending on the purpose, the spatial scale, and the accuracy on input data. In this work, we decided to aggregate results at slope unit level – with a simple average of grid rockfall

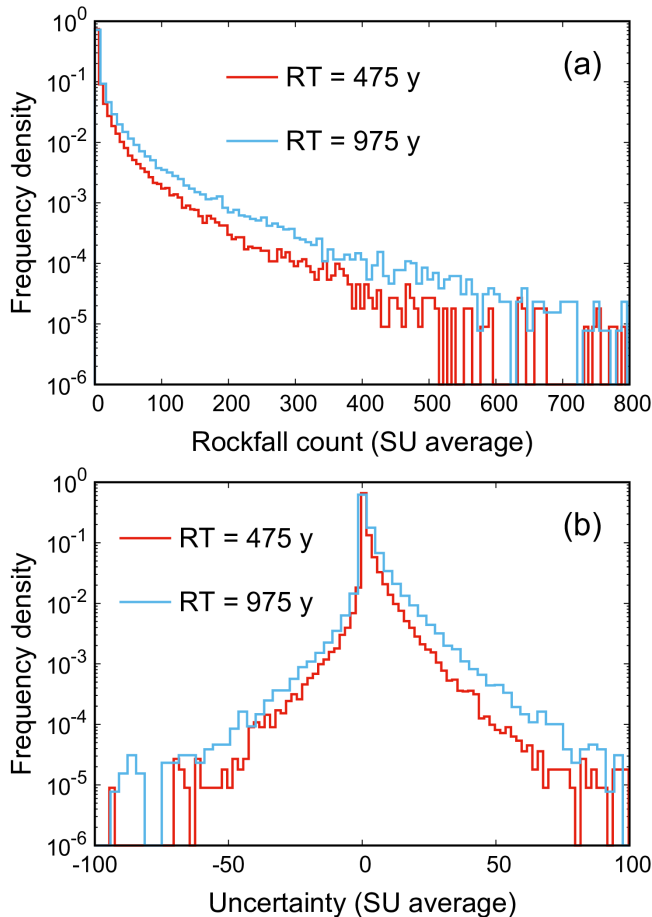


Figure 9: The distributions of rockfall trajectory count values (a) and of uncertainty values (b), averaged at slope unit level, for the two return times (RT) considered in this work. The distribution in (a) allows for a head/tail break classification, which we used for the left maps in **Figs. 5-8**, while the absolute values of the distribution in (b) was classified with the same method, for the right maps in the same figures; negative values in (b) are 7,240, out of a total of 111,219 non-null values.

trajectory count per SU polygon. Slope units relate in a straightforward way with the real world topography, and are more suited for national scale zonations than the original 10 m x 10 m grid. On the other hand, one can look directly at grid cells results, if the interest is on a specific medium- or small-scale area and, possibly, if input data (DEM and geomorphological information on the sources) can be replaced with higher resolution ones. Studies at intermediate (regional) scale within the same approach are underway and will be published elsewhere; an application of the general method proposed here, at small (local) scale, was recently published by **Alvioli et al. (2022b)**.

Second, use of a grid-based, physically based approach allows introducing a temporal dependence, even if the specific model does not explicitly contain a temporal component, nor a mechanism to model the triggering conditions that generate landslides – rockfalls, in the case of STONE.

The novel modeling framework introduced in this work and illustrated in **Fig. 1** is one possible example of exploiting such a possibility. Knowledge of spatial distribution of the strength of the triggering phenomenon – in this case, ground motion – allows adding a temporal component on top of the “static” simulations provided by the model as is. This is often implemented in hazard models using estimated landslide frequency relations; here, we proposed an alternative, simple approach. A magnitude component is also contained in the model STONE, in principle, but we decided not to exploit that feature in this work, to explore only the introduction of different return times. Recently, statistical models appeared that predict the aggregated size of landslides, in addition to spatial likelihood (**Di Napoli et al., 2022**), but certainly there is no standard approach to do that, yet.

7 Conclusions

Physically based rockfall simulations are usually performed in a time-independent fashion, and result in susceptibility maps whose content is limited to the relative spatial likelihood of rockfall occurrence, with a few notable exceptions. In this work we introduced a new modeling framework to obtain the best approximation, with the available data and tools, to seismically induced rockfall hazard for different return times in Italy. The proposed framework, summarized in **Fig. 1**, includes heterogeneous data and models, combined in successive steps and, most notably, with the introduction of a novel approach to use ground shaking maps to infer scenario-based triggering of static rockfall sources, otherwise obtained solely from morphometric analysis. This study allows drawing the following conclusions.

- The overall conceptual and computational framework can be effectively applied on the whole of Italy on a 10 m grid. This is a relatively high resolution for a national-scale application; nevertheless, the results produced here were aggregated at (coarser) slope unit level, for ease of interpretation and to mitigate the effect of inaccuracies and approximations.
- A novel, simple seismic trigger model can be devised to link ground shaking and activation of rockfall sources, in rockfall-prone areas. The model maps peak ground acceleration values into a probability of source activation, which in turn is the main ingredient to simulate geometrical trajectories using the model STONE. Similar or more advanced physical models in principle can use the same input. Additional functional forms for the mapping of PGA into probabilities can be similarly explored.
- Seismic shake maps for different return times help calibrating a dynamic trigger; here, we considered two different return times. In principle, additional return times can be considered with little modification (cal-

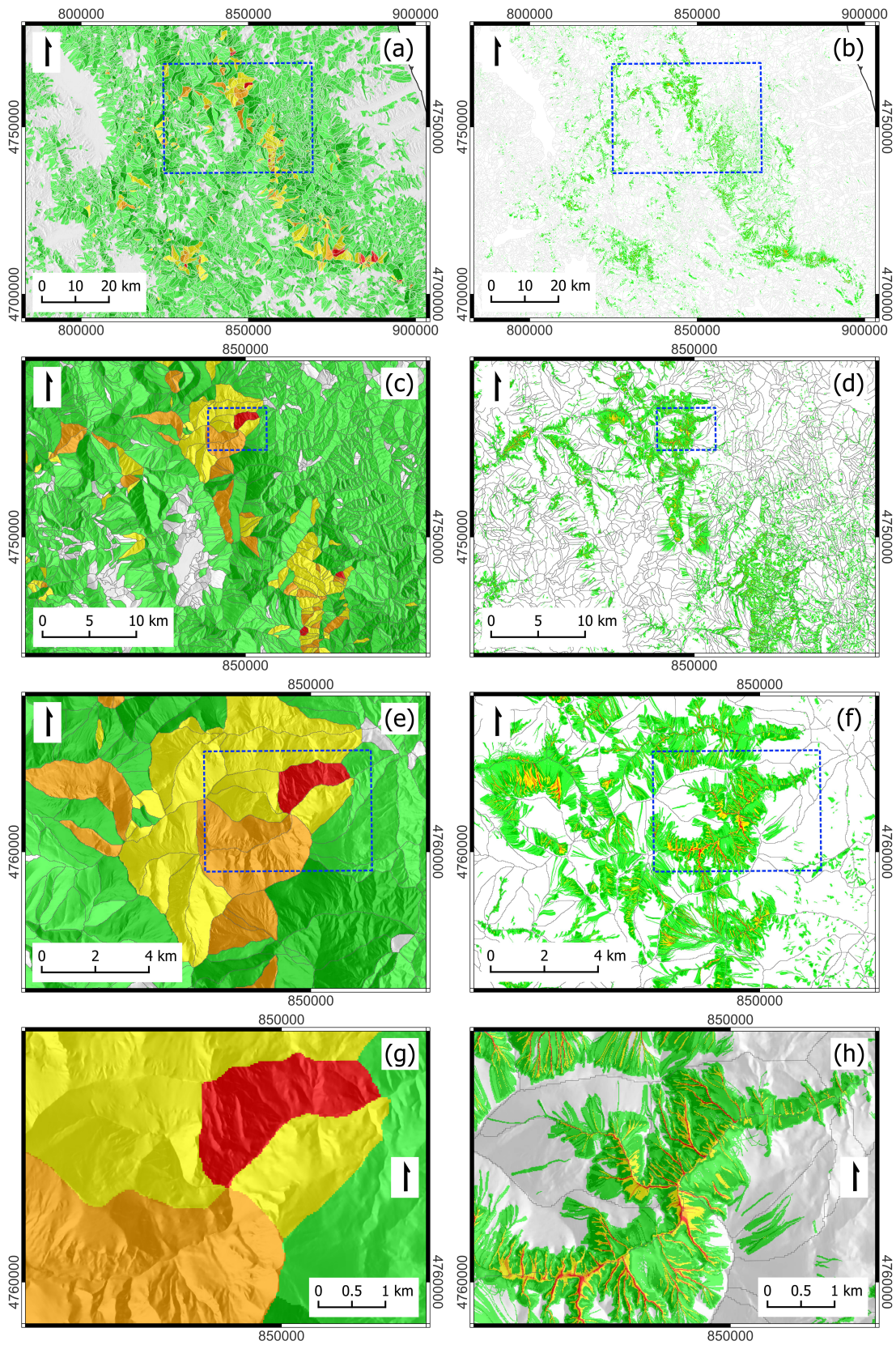


Figure 10: Comparison of slope unit average *vs.* actual rockfall count, at increasing zoom level, top to bottom; (a) is the same as **Fig. 6(a)**. Left figures – (a), (c), (e) and (g) – show results aggregated at slope unit level (as in all of the other figures in this work), while figures in the right – (b), (d), (f) and (h) – show the corresponding rockfall count maps, at the same zoom level, before averaging, classified with head/tail breaks as well. Blue rectangles show the extent of the next zoom level.

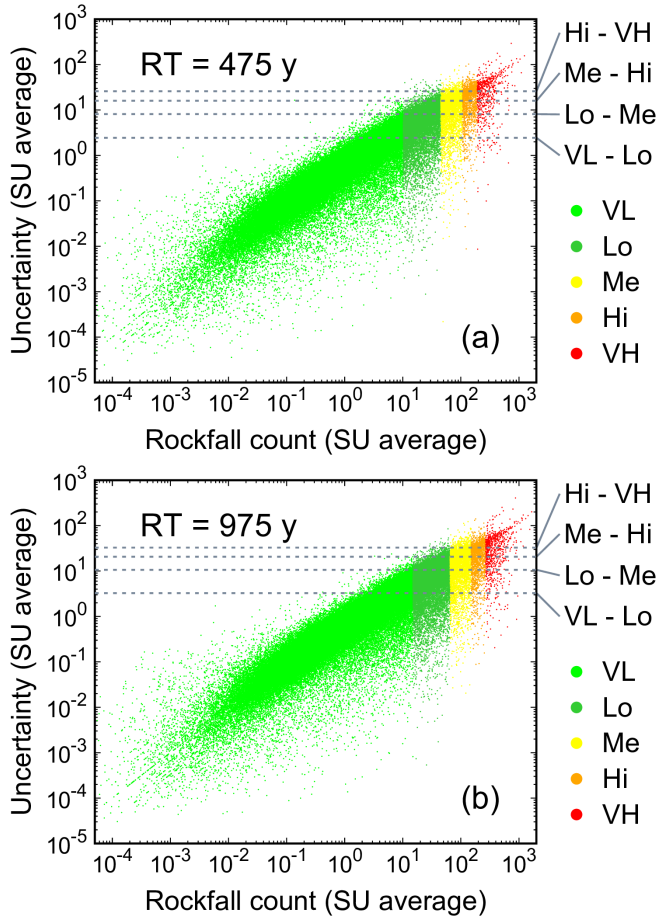


Figure 11: Relationship between the trajectory count and uncertainty, both averaged at slope unit level, for the two different return times considered here. The different colors correspond to the five classes of trajectory count, used in all of the figures (maps) shown in this work, and the horizontal lines correspond to the breaks used to define uncertainty values, which are different in (a) and in (b), as well as in all the other figures.

ibration), and a hazard can be calculated for a wider range of temporal component. We found that the main difference between the 475 y and 975 y return times is mostly about the extent of the area where hazard is not null, and that uncertainty grows substantially with growing hazard.

- We judge the results robust, in that we found no obvious correlations in hazard values *vs.* slope angle, and in hazard values *vs.* peak ground acceleration values – suggesting the main inputs of the modeling chain cannot be easily disentangled, and both contribute to the complexity of the output maps.

Possibilities offered by the same approach include real-time assessment of rockfall hazard. Replacing the F_{RT} dependence on return time, in the model $P_{trigger}(S, PGA) = P_{static}(S) F_{RT}(PGA)$, with a real-time ground shaking map PGA would require proper calibration on

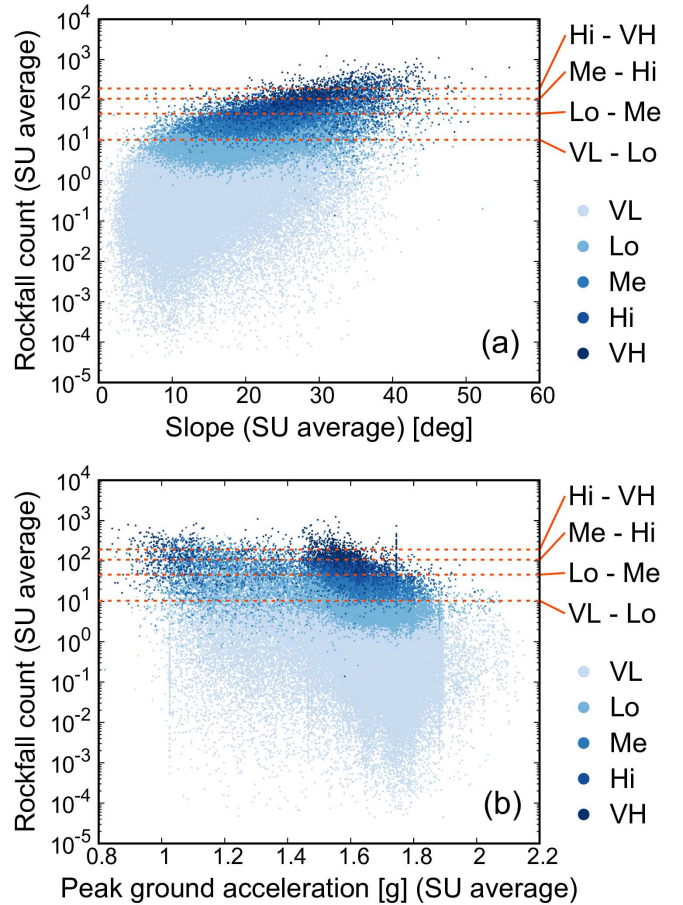


Figure 12: Scatter plots of trajectory count (*i.e.*, the STONE output) *vs.* slope angle (a) and *vs.* peak ground acceleration, in units of g (b). All quantities averaged at slope unit level; STONE results and PGA corresponding to $RT = 475$ y. Dots correspond to individual slope units. Colors match those of the uncertainty class the slope unit (as in **Fig. 5**) and horizontal dotted lines correspond to the separation into susceptibility classes (as in **Fig. 5** and **Table 4**).

different events occurred in Italy, which is possible but beyond the scope of this work. Additional calibration, with accurate data, would also allow to specify different functional forms for the $F(PGA)$ model. In fact, the linear model for $F(PGA)$ adopted here is the simplest choice for mapping PGA values into the $[0, 1]$ interval required by the formulation of the model, but different functional forms may show better predictive performance, which was not assessed for specific events, here.

In conclusion, we believe that the new model for seismic triggering of rockfall simulations seems promising; in this case it was calibrated within the range of PGA values spanned by the maps for two return times, but possibilities go beyond that. Eventually, we stress that an “absolute” model – *i.e.*, a model which would work in real-time for any earthquake event, would require corresponding map-

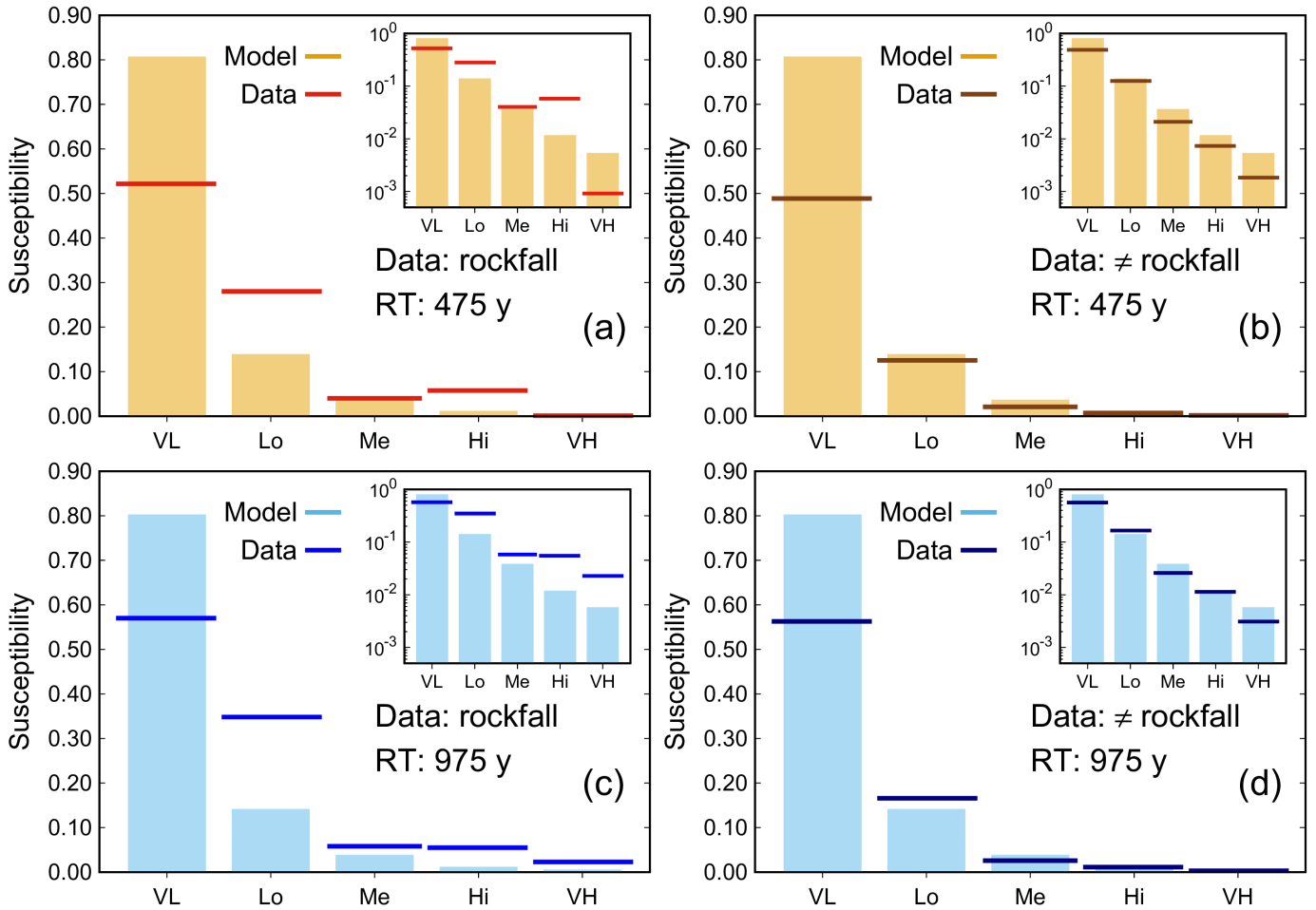


Figure 13: Partial validation of the hazard maps obtained in this work, **Fig. 5**, using the CEDIT (point) inventory of seismically-induced landslides. (a)-(c) data for rockfalls; (b)-(d) data for any other kind of landslides, including unclassified points. Model results are always for rockfalls, studies in this work: (a)-(b) model results for $RT=475$ y; (c)-(d) model results for $RT=975$ y. The insets show the same plot as in the larger boxes, but in logarithmic scale. The apparent difference between RTs in “Data” proportions is due to the different spatial distribution of each class. VL: very low; Lo= low; Me: medium; Hi: high; VH: very high.

ping of “absolute” PGA values, which is still not available to us but work in this direction is under way.

8 Data availability

Maps obtained in this research can be visualized with the WebGIS available on the web page of the project *Multiscale methods for the zonation of seismically-induced landslide hazard in Italy*, <https://frasi-project.irpi.cnr.it/>, and are available for download in vector format at the main slope units project page, <https://geomorphology.irpi.cnr.it/tools/slope-units>. The maps proposed in this work are encompassed by the bounding box 36.40866N–47.11408N and 19.5446E–6.502227E (EPSG:4326), covering the whole of Italy.

9 Acknowledgments

We thank the Italian Ministry of Environment and Ecological Transition (MATTM - *Ministero dell’ambiente e della tutela del territorio e del mare*, now MITE *Ministero dell’Ambiente e della Transizione Ecologica*) for partially supporting this research within the project FRA.SI - *Multiscale methods for the zonation of seismically-induced landslide hazard in Italy*.

References

Federico Agliardi and Giovanni B. Crosta. High resolution three-dimensional numerical modelling of rockfalls. *International Journal of Rock Mechanics and Mining Sciences*, 40(4):455–471, 2003. ISSN 1365-1609. doi: 10.1016/S1365-1609(03)00021-2.

Massimiliano Alvioli, Ivan Marchesini, Paola Reichenbach,

- Mauro Rossi, Francesca Ardizzone, Federica Fiorucci, and Fausto Guzzetti. Automatic delineation of geomorphological slope units with `r.slopeunits v1.0` and their optimization for landslide susceptibility modeling. *Geoscientific Model Development*, 9(11):3975–3991, 2016. doi: 10.5194/gmd-9-3975-2016.
- Massimiliano Alvioli, Massimo Melillo, Fausto Guzzetti, Mauro Rossi, Elisa Palazzi, Jost von Hardenberg, Maria Teresa Brunetti, and Silvia Peruccacci. Implications of climate change on landslide hazard in Central Italy. *Science of The Total Environment*, 630:1528–1543, 2018. ISSN 0048–9697. doi: 10.1016/j.scitotenv.2018.02.315.
- Massimiliano Alvioli, Fausto Guzzetti, and Ivan Marchesini. Parameter-free delineation of slope units and terrain subdivision of Italy. *Geomorphology*, 358:107124, 2020. ISSN 0169–555X. doi: 10.1016/j.geomorph.2020.107124.
- Massimiliano Alvioli, Michele Santangelo, Federica Fiorucci, Mauro Cardinali, Ivan Marchesini, Paola Reichenbach, Mauro Rossi, Fausto Guzzetti, and Silvia Peruccacci. Rockfall susceptibility and network-ranked susceptibility along the Italian railway. *Engineering Geology*, 293:106301, 2021. ISSN 0013–7952. doi: 10.1016/j.enggeo.2021.106301.
- Massimiliano Alvioli, Ivan Marchesini, Badal Pokharel, Kaushal Gnyawali, and Samsung Lim. Geomorphological slope units of the Himalayas. *Journal of Maps*, 2022a. doi: 10.1080/17445647.2022.2052768.
- Massimiliano Alvioli, Ada De Matteo, Raffaele Castaldo, Pietro Tizzani, and Paola Reichenbach. Three-dimensional simulations of rockfalls in Ischia, Southern Italy, and preliminary susceptibility zonation. *Geomatics, Natural Hazards and Risk*, 13(1):2712–2736, 2022b. doi: 10.1080/19475705.2022.2131472.
- Gabriele Amato, Matteo Fiorucci, Salvatore Martino, Luigi Lombardo, and Lorenzo Palombi. Earthquake-triggered landslide susceptibility in Italy by means of artificial neural network. *Earth ArXiv*, 2021. doi: 10.31223/X59W39. Preprint.
- Dominic Assimaki, George Gazetas, and Eduardo Kausel. Effects of Local Soil Conditions on the Topographic Aggravation of Seismic Motion: Parametric Investigation and Recorded Field Evidence from the 1999 Athens Earthquake. *Bulletin of the Seismological Society of America*, 95(3):1059–1089, 2005. ISSN 0037-1106. doi: 10.1785/0120040055.
- Maria Sole Benigni, Fabrizio Brammerini, Gianluca Carbone, Sergio Castenetto, Gian Paolo Cavinato, Monia Coltella, Margherita Giuffrè, Massimiliano Moscatelli, Giuseppe Naso, Andrea Pietrosante, and Francesco Stigliano. Studi di microzonazione sismica in Italia. Technical report, DPC – Dipartimento della Protezione Civile, commissione tecnica per il supporto e monitoraggio degli studi di Microzonazione Sismica (ex art.5, OPCM3907/10) – WebMs; WebCLE, 2018. URL <https://www.webms.it/>. *In Italian*.
- Alfonso Bosellini. *Outline of the Geology of Italy*, pages 21–27. Springer International Publishing, Cham, 2017. ISBN 978-3-319-26194-2. doi: 10.1007/978-3-319-26194-2.3.
- George D. Bouckovalas and Achilleas G. Papadimitriou. Numerical evaluation of slope topography effects on seismic ground motion. *Soil Dynamics and Earthquake Engineering*, 25(7):547–558, 2005. ISSN 0267–7261. doi: 10.1016/j.soildyn.2004.11.008. 11th International Conference on Soil Dynamics and Earthquake Engineering (ICSDEE): Part 1.
- Francesco Bucci, Michele Santangelo, Lorenzo Fongo, Massimiliano Alvioli, Mauro Cardinali, Laura Melelli, and Ivan Marchesini. A new digital lithological map of Italy at 1:100,000 scale for geo-mechanical modelling. *Earth System Science*, pages 1–35, 2022. doi: 10.5194/essd-2022-26. *In press*.
- Patrizia Caprari, Marta Della Seta, Salvatore Martino, Andrea Fantini, Matteo Fiorucci, and Tiziana Priore. Upgrade of the CEDIT database of earthquake-induced ground effects in Italy. *Italian Journal of Engineering Geology and Environment*, 2:23–29, 2018. doi: 10.4408/IJEGE.2018-02.O-02.
- Fu Chu Dai, Chong Xu, Xin Yao, Ling Xu, Xin Bin Tu, and Qiu Ming Gong. Spatial distribution of landslides triggered by the 2008 Ms 8.0 Wenchuan earthquake, China. *Journal of Asian Earth Sciences*, 40(4):883–895, 2011. ISSN 1367-9120. doi: 10.1016/j.jseaes.2010.04.010.
- Mariano Di Napoli, Hakan Tanyas, Daniela Castro-Camilo, Domenico Calcaterra, Andrea Cevasco, Diego Di Martire, Giacomo Pepe, Pierluigi Brandolini, and Luigi Lombardo. On the estimation of landslide intensity, hazard and density via data-driven models. *Earth ArXiv*, 2022. doi: 10.31223/X52D1J. Preprint.
- Guillem Doménech, Massimiliano Alvioli, and Jordi Corominas. Preparing first-time slope failures hazard maps: from pixel-based to slope unit-based. *Landslides*, 17:249–265, 2020. ISSN 1612–510X. doi: 10.1007/s10346-019-01279-4.
- Luuk Dorren, Frédéric Berger, Franck Bourrier, Nicolas Eckert, Charalampos Saroglou, Massimiliano Schwarz, Markus Stoffel, Daniel Trappmann, Hans-Heini Utelli, and Christine Moos. Delimiting rockfall runout zones using reach probability values simulated with a Monte-Carlo based 3D trajectory model. *Natural Hazards and Earth System Sciences Discussions*, pages 1–23, 2022. doi: 10.5194/nhess-2022-32.
- Gaetano Falcone, Gianluca Acunzo, Amerigo Mendicelli,

- Federico Mori, Giuseppe Naso, Edoardo Peronace, Attilio Porchia, Gino Romagnoli, Emanuele Tarquini, and Massimiliano Moscatelli. Seismic amplification maps of Italy based on site-specific microzonation dataset and one-dimensional numerical approach. Engineering Geology, 289:106170, 2021. ISSN 0013-7952. doi: 10.1016/j.enggeo.2021.106170.
- Xuanmei Fan, Gianvito Scaringi, Oliver Korup, A. Joshua West, Cees J. van Westen, Hakan Tanyaş, Niels Hovius, Tristram C. Hales, Randall W. Jibson, Kate E. Allstadt, Limin Zhang, Stephen G. Evans, Chong Xu, Gen Li, Xiangujun Pei, Qiang Xu, and Runqiu Huang. Earthquake-induced chains of geologic hazards: Patterns, mechanisms, and impacts. Reviews of Geophysics, 57(2):421–503, 2019. doi: 10.1029/2018RG000626.
- Francisco José Fernández, Rosana Menéndez-Duarte, Luis Pando, Laura Rodríguez-Rodríguez, and Miguel Iglesias. Gravitational slope processes triggered by past earthquakes on the Western Cantabrian Mountains (Sierra de la Sobia, Northern Spain). Geomorphology, 390:107867, 2021. ISSN 0169-555X. doi: 10.1016/j.geomorph.2021.107867.
- Lorenzo Fongo. Verso una nuova carta litologica d’Italia in scala 1:100,000. Master Thesis, University of Perugia. *In Italian*, 2018.
- Simona Fratianni and Fiorella Acquavota. The Climate of Italy, pages 29–38. Springer International Publishing, Cham, 2017. ISBN 978-3-319-26194-2. doi: 10.1007/978-3-319-26194-2_4.
- Fausto Guzzetti and Paola Reichenbach. Towards a definition of topographic divisions for Italy. Geomorphology, 11(1):57–74, 1994. ISSN 0169-555X. doi: 10.1016/0169-555X(94)90042-6.
- Fausto Guzzetti, Giovanni Crosta, Riccardo Detti, and Federico Agliardi. STONE: a computer program for the three-dimensional simulation of rock-falls. Computers & Geosciences, 28(9):1079 – 1093, 2002. ISSN 0098-3004. doi: 10.1016/S0098-3004(02)00025-0.
- Fausto Guzzetti, Paola Reichenbach, and Gerald F. Wieczorek. Rockfall hazard and risk assessment in the Yosemite Valley, California, USA. Natural Hazards and Earth System Sciences, 3(6):491–503, 2003. doi: 10.5194/nhess-3-491-2003.
- Fausto Guzzetti, Paola Reichenbach, and Silvia Ghigi. Rockfall hazard and risk assessment along a transportation corridor in the Nera Valley, Central Italy. Environmental Management, 34(2):191–208, Aug 2004. ISSN 1432-1009. doi: 10.1007/s00267-003-0021-6.
- Edwin L. Harp, David K. Keefer, Hiroshi P. Sato, and Hiroshi Yagi. Landslide inventories: The essential part of seismic landslide hazard analyses. Engineering Geology, 122(1):9–21, 2011. ISSN 0013-7952. doi: 10.1016/j.enggeo.2010.06.013.
- Hanne Hendrickx, Gaele Le Roy, Agnes Helmstetter, Eric Pointner, Eric Larose, Luc Braillard, Jan Nyssen, Reynald Delaloye, and Amaury Frankl. Timing, volume and precursory indicators of rock- and cliff fall on a permafrost mountain ridge (Mattertal, Switzerland). Earth Surface Processes and Landforms, 47(6):1532–1549, 2022. ISSN 0197-9337. doi: 10.1002/esp.5333.
- Runqiu Huang, Qiang Xu, and Junjie Huo. Mechanism and geo-mechanics models of landslides triggered by 5.12 Wenchuan earthquake. Journal of Mountain Science, 8:200–210, 2011. doi: 10.1007/s11629-011-2104-9.
- Junko Iwahashi, Izumi Kamiya, Masashi Matsuoka, and Dai Yamazaki. Global terrain classification using 280 m DEMs: segmentation, clustering, and reclassification. Progress in Earth and Planetary Science, 5(1):1, Jan 2018. ISSN 2197-4284. doi: 10.1186/s40645-017-0157-2.
- Liesbet Jacobs, Matthieu Kervyn, Paola Reichenbach, Mauro Rossi, Ivan Marchesini, Massimiliano Alvioli, and Olivier Dewitte. Regional susceptibility assessments with heterogeneous landslide information: Slope unit- vs. pixel-based approach. Geomorphology, 356:107084, 2020. ISSN 0169-555X. doi: 10.1016/j.geomorph.2020.107084.
- Christopher L. Jones, Jerry D. Higgins, and Richard D. Andrew. MI-66 Colorado Rockfall Simulation Program, version 4.0. Technical report, Colorado Geological Survey, Division of Minerals and Geology, Department of Natural Resources, 2000. URL <https://coloradogeologicalsurvey.org/publications/colorado-rockfall-simulation-program>.
- Mor Kanari, Oded Katz, Ram Weinberger, Naomi Porat, and Shmuel Marco. Evaluating earthquake-induced rockfall hazard near the Dead Sea Transform. Natural Hazards and Earth System Sciences, 19(4):889–906, 2019. doi: 10.5194/nhess-19-889-2019.
- David K. Keefer. Investigating landslides caused by earthquakes - A historical review. Surveys in Geophysics, 23: 473–510, 2002. doi: 10.1023/A:1021274710840.
- Albert R. Kottke, Xiaoyue Wang, and Ellen M. Rathje. Technical manual for strata. Technical report, University of Texas, 2013. URL <https://github.com/arkottke/strata>.
- Marco Loche, Massimiliano Alvioli, Ivan Marchesini, Haakon Bakka, and Luigi Lombardo. Landslide susceptibility maps of Italy: lesson learnt from dealing with multiple landslide classes and the uneven spatial distribution of the national inventory. Earth-Science Reviews, 232:104125, 2022a. doi: 10.1016/j.earscirev.2022.104125.
- Marco Loche, Gianvito Scaringi, Ali P. Yunus, Filippo Catani, Hakan Tanyaş, William Frodella, Xuanmei

- Fan, and Luigi Lombardo. Surface temperature controls the pattern of post-earthquake landslide activity. Scientific Reports, 12(988), 2022b. doi: 10.1038/s41598-022-04992-8.
- Luigi Lombardo and Hakan Tanyaş. From scenario-based seismic hazard to scenario-based landslide hazard: fast-forwarding to the future via statistical simulations. Stochastic Environmental Research and Risk Assessment, 2021. doi: 10.1007/s00477-021-02020-1.
- Juan López-Vinielles, José A. Fernández-Merodo, Pablo Ezquerro, Juan C. García-Davalillo, Roberto Sarro, Cristina Reyes-Carmona, Anna Barra, José A. Navarro, Vrinda Krishnakumar, Massimiliano Alvioli, and Gerardo Herrera. Combining satellite InSAR, slope units and finite element modeling for stability analysis in mining waste disposal areas. Remote Sensing, 13(10), 2021. ISSN 2072-4292. doi: 10.3390/rs13102008.
- Odin Marc, Niels Hovius, Patrick Meunier, Taro Uchida, and Shin-ichiro Hayashi. Transient changes of landslide rates after earthquakes. Geology, 43(10):883–886, 10 2015. ISSN 0091-7613. doi: 10.1130/G36961.1.
- Ivan Marchesini, Mauro Rossi, Massimiliano Alvioli, Michele Santangelo, and Mauro Cardinali. Slope-catchment area relationship for debris-flow source area identification. In Massimiliano Alvioli, Ivan Marchesini, Laura Melelli, Peter Guth, and Scott Peckham, editors, Proceedings of the sixth Geomorphometry conference: Geomorphometry 2020, Perugia, Italy, 2020. CNR Edizioni, Rome. doi: 10.30437/geomorphometry2020\47.
- Ivan Marchesini, Paola Salvati, Mauro Rossi, Marco Donini, Simone Sterlacchini, and Fausto Guzzetti. Data-driven flood hazard zonation of Italy. Journal of Environmental Management, 294:112986, 2021. ISSN 0301-4797. doi: 10.1016/j.jenvman.2021.112986.
- Salvatore Martino, Adriano Prestininzi, and R. W. Romeo. Earthquake-induced ground failures in Italy from a reviewed database. Natural Hazards and Earth System Sciences, 14(4):799–814, 2014. doi: 10.5194/nhess-14-799-2014.
- Chris Massey, Fernando della Pasqua, Caroline Holden, Anna Kaiser, Laurie Richards, Joseph Wartman, Mauri J. McSaveney, Garth Archibald, Mark D. Yetton, and Lukáš Jankøu. Rock slope response to strong earthquake shaking. Landslides, 14:249–268, 2017. doi: 10.1007/s10346-016-0684-8.
- Chris I. Massey, Mauri J. McSaveney, Tony Taig, Laurie Richards, Nicola J. Litchfield, David A. Rhoades, Graeme H. McVerry, Biljana Lukovic, David W. Heron, William Ries, and Russ J. Van Dissen. Determining rockfall risk in christchurch using rockfalls triggered by the 2010-2011 canterbury earthquake sequence. Earthquake Spectra, 30:155–181, 2014. ISSN 8755-2930. doi: 10.1193/021413EQS026M.
- Chris I. Massey, Michael J. Olsen, Joseph Wartman, Andrew Senogles, Biljana Lukovic, Ben A. Leshchinsky, Garth Archibald, Nicola Litchfield, Russ Van Dissen, Saskia de Vilder, and Caroline Holden. Rockfall activity rates before, during and after the 2010/2011 Canterbury earthquake sequence. Journal of Geophysical Research: Earth Surface, 127(3):e2021JF006400, 2022. doi: 10.1029/2021JF006400.
- Gerard Matas, Nieves Lantada, Jordi Corominas, Josep A. Gili, Roger Ruiz-Carulla, and Albert Prades. RockGIS: a GIS-based model for the analysis of fragmentation in rockfalls. Landslides, 14:1565–1578, 2017. doi: 10.1007/s10346-017-0818-7.
- Olga Mavrouli and Jordi Corominas. Evaluation of maximum rockfall dimensions based on probabilistic assessment of the penetration of the sliding planes into the slope. Rock Mechanics and Rock Engineering, 53: 2301–2312, 2020. ISSN 0723-2632. doi: 10.1007/s00603-020-02060-z.
- Olga Mavrouli, Jordi Corominas, and Joseph Wartman. Methodology to evaluate rock slope stability under seismic conditions at Solà de Santa Coloma, Andorra. Natural Hazards and Earth System Sciences, 9(6): 1763–1773, 2009. ISSN 1561-8633. doi: 10.5194/nhess-9-1763-2009.
- Paola Mazzoglio, Ilaria Butera, Massimiliano Alvioli, and Pierluigi Claps. The role of morphology on the spatial distribution of short-duration rainfall extremes in Italy. Hydrology and Earth System Sciences, 26:1–16, 2021. doi: 10.5194/hess-2021-503.
- Carlo Meletti and Valentina Montaldo. Stime di pericolosità sismica per diverse probabilità di superamento in 50 anni: valori di ag. Technical Report Deliverable D2, Progetto DPC-INGV S1, 2007. URL <http://esse1.mi.ingv.it/d2.html>. In *Italian*.
- Amerigo Mendicelli, Gaetano Falcone, Gianluca Acunzo, Federico Mori, Giuseppe Naso, Edoardo Peronace, Attilio Porchia, Gino Romagnoli, and Massimiliano Moscatelli. Italian seismic amplification factors for peak ground acceleration and peak ground velocity. Journal of Maps, pages 1–11, 2022. doi: 10.1080/17445647.2022.2101947.
- Valentina Montaldo and Carlo Meletti. Valutazione del valore della ordinata spettrale a 1 sec e ad altri periodi di interesse ingegneristico. Technical Report Deliverable D3, Progetto DPC-INGV S1, 2007. URL <http://esse1.mi.ingv.it/d3.html>. In *Italian*.
- Federico Mori, Amerigo Mendicelli, Massimiliano Moscatelli, Gino Romagnoli, Edoardo Peronace, and Giuseppe Naso. A new Vs30 map for Italy based on the seismic microzonation dataset. Engineering Geology, 275:105745, 2020. ISSN 0013-7952. doi: 10.1016/j.enggeo.2020.105745.

- Farrokh Nadim. Hazard. Encyclopedia of Natural Hazards, pages 425–426, 2013. doi: 10.1007/978-1-4020-4399-4_164.
- Martha Anna Nowicki Jessee, Michael W. Hamburger, Kate Allstadt, David J. Wald, Scott M. Robeson, Hakan Tanyaş, Mike Hearne, and Eric M. Thompson. A global empirical model for near–real–time assessment of seismically induced landslides. Journal of Geophysical Research: Earth Surface, 123(8):1835–1859, 2018. doi: 10.1029/2017JF004494.
- María Amparo Núñez-Andrés, Nieves Lantada Zarzosa, and José Martínez-Llario. Spatial data infrastructure (SDI) for inventory rockfalls with fragmentation information. Natural Hazards, 2022. ISSN 1573-0840. doi: 10.1007/s11069-022-05282-2. *In press*.
- María Amparo Núñez-Andrés, Albert Prades-Valls, Gerard Matas, Felipe Buill, and Nieves Lantada. New approach for photogrammetric rock slope premonitory movements monitoring. Remote Sensing, 15(2), 2023. doi: 10.3390/rs15020293.
- Lewis A. Owen, Ulrich Kamp, Ghazanfar A. Khattak, Edwin L. Harp, David K. Keefer, and Mark A. Bauer. Landslides triggered by the 8 October 2005 Kashmir earthquake. Geomorphology, 94(1):1–9, 2008. ISSN 0169-555X. doi: 10.1016/j.geomorph.2007.04.007.
- Antonio Pignalosa, Giovanni Forte, Paolo Budetta, and Antonio Santo. Topographic amplification and debris remobilization as a cause for increasing rockfall hazard in seismic areas: A case study in Central Italy. Geomorphology, 403, 2022. ISSN 0169-555X. doi: 10.1016/j.geomorph.2022.108160.
- Badal Pokharel, Massimiliano Alvioli, and Samsung Lim. Assessment of earthquake–induced landslide inventories and susceptibility maps using slope unit–based logistic regression and geospatial statistics. Scientific Reports, 11:21333, 2021. ISSN 2045-2322. doi: 10.1038/s41598-021-00780-y.
- Saverio Romeo, Lucio Di Matteo, Laura Melelli, Corrado Cencetti, Walter Dragoni, and Andrea Fredduzzi. Seismic–induced rockfalls and landslide dam following the October 30, 2016 earthquake in Central Italy. Landslides, 14(4):1457–1465, 2017. ISSN 1612-510X. doi: 10.1007/s10346-017-0841-8.
- Michele Santangelo, Massimiliano Alvioli, Marco Baldo, Mauro Cardinali, Daniele Giordan, Fausto Guzzetti, Ivan Marchesini, and Paola Reichenbach. Brief communication: Remotely piloted aircraft systems for rapid emergency response: Road exposure to rockfall in Villanova di Accumoli (Central Italy). Natural Hazards and Earth System Sciences, 19(2):325–335, 2019. doi: 10.5194/nhess-19-325-2019.
- Massimiliano Stucchi, Carlo Meletti, Valentina Montaldo, Aybige Akinci, Ezio Faccioli, Paolo Gasperini, Luca Malagnini, and Gianluca Valensise. *Pericolosità sismica di riferimento per il territorio nazionale MPS04* [data set]. Istituto Nazionale di Geofisica e Vulcanologia (INGV), 2004. doi: 10.13127/sh/mps04/ag. Dataset.
- Hakan Tanyaş, Mauro Rossi, Massimiliano Alvioli, Cees J. van Westen, and Ivan Marchesini. A global slope unit-based method for the near real-time prediction of earthquake-induced landslides. Geomorphology, 327: 126–146, 2019a. ISSN 0169-555X. doi: 10.1016/j.geomorph.2018.10.022.
- Hakan Tanyaş, Cees J. van Westen, Claudio Persello, and Massimiliano Alvioli. Rapid prediction of the magnitude scale of landslide events triggered by an earthquake. Landslides, 16(4):661–676, Apr 2019b. ISSN 1612-5118. doi: 10.1007/s10346-019-01136-4.
- Simone Tarquini, Ilaria Isola, Massimiliano Favalli, Francesco Mazzarini, Marina Bisson, Maria Teresa Pareschi, and Enzo Boschi. TINITALY/01: a new triangular irregular network of Italy. Annales Geophysicae, 50:407–425, 2007. doi: 10.4401/ag-4424.
- Andrea Valagussa, Paolo Frattini, and Giovanni B. Crosta. Earthquake–induced rockfall hazard zoning. Engineering Geology, 182:213–225, 2014. ISSN 0013-7952. doi: 10.1016/j.enggeo.2014.07.009.
- Andrea Valagussa, Odin Marc, Paolo Frattini, and Giovanni Battista Crosta. Seismic and geological controls on earthquake–induced landslide size. Earth and Planetary Science Letters, 506:268–281, 2019. ISSN 0012-821X. doi: 10.1016/j.epsl.2018.11.005.
- Nan Wang, Weiming Cheng, Mattia Marconcini, Felix Bachofer, Changjun Liu, Junnan Xiong, and Luigi Lombardo. Space–time susceptibility modeling of hydro–morphological processes at the Chinese national scale. Engineering Geology, 301:106586, 2022. ISSN 0013-7952. doi: https://doi.org/10.1016/j.enggeo.2022.106586.
- Ying Wang, Chongzhen Song, Qigen Lin, and Juan Li. Occurrence probability assessment of earthquake–triggered landslides with Newmark displacement values and logistic regression: The Wenchuan earthquake, China. Geomorphology, 258:108–119, 2016. ISSN 0169-555X. doi: 10.1016/j.geomorph.2016.01.004.
- Emmanuel Wick, Valérie Baumann, and Michel Jaboyedoff. Report on the impact of the 27 February 2010 earthquake (Chile, M-w 8.8) on rockfalls in the Las Cuevas valley, Argentina. Natural Hazards and Earth System Sciences, 10(9):1989–1993, 2010. ISSN 1561-8633. doi: 10.5194/nhess-10-1989-2010.
- Shui Yamaguchi and Mio Kasai. A new index representative of seismic cracks to assess post–seismic landslide susceptibility. Transactions in GIS, 26(2):1040–1061, 2022. doi: 10.1111/tgis.12900.